

1 **Dynamical MJO forecasts using an ensemble subseasonal-to-seasonal**
2 **forecast system of the IAP-CAS model**

3 Yangke Liu^{1,6}, Qing Bao^{*1}, Bian He¹, Xiaofei Wu², Jing Yang³, Yimin Liu¹, Guoxiong Wu¹, Tao Zhu¹,
4 Siyuan Zhou¹, Yao Tang^{1,6}, Ankang Qu^{1,7}, Yalan Fan³, Anling Liu³, Dandan Chen^{1,6}, Zhaoming Luo^{1,7},
5 Xing Hu⁴, Tongwen Wu⁵

6 ¹State Key Laboratory of Numerical Modeling for Atmospheric Sciences and Geophysical Fluid Dynamics (LASG), Institute
7 of Atmospheric Physics, Chinese Academy of Sciences, Beijing 100029, China

8 ²School of Atmospheric Sciences/Plateau Atmosphere and Environment Key Laboratory of Sichuan Province, Chengdu
9 University of Information Technology, Chengdu 610225, China

10 ³Faculty of Geographical Science, Beijing Normal University, Beijing 100875, China

11 ⁴National Meteorological Information Center, China Meteorological Administration, Beijing 100081, China

12 ⁵Center for Earth System Modeling and Prediction, China Meteorological Administration, Beijing 100081, China

13 ⁶College of Earth and Planetary Sciences, University of Chinese Academy of Science, Beijing 100049, China

14 ⁷School of Emergency Management Science and Engineering, University of Chinese Academy of Science, Beijing 100049,
15 China

16 *Correspondence to:* Qing Bao (baoqing@mail.iap.ac.cn)

17 **Abstract.** The Madden-Julian Oscillation (MJO) is a crucial predictability source on a sub-seasonal to seasonal (S2S) timescale.
18 Therefore, the models participating in the WWRP/WCRP S2S prediction project focus on accurately predicting and analyzing
19 the MJO. This study provided a detailed description of the configuration within the IAP-CAS S2S forecast system. We assessed
20 the accuracy of the IAP-CAS model's MJO forecast using traditional RMM analysis and cluster analysis. Then, we explained
21 the reasons behind any bias observed in the MJO forecast. Comparing the 20-year hindcast with observations, we found that
22 the IAP-CAS ensemble mean has a skill of 24 days. However, the ensemble spread still has potential for improvement. To
23 examine the MJO structure in detail, we used cluster analysis to classify the MJO events during boreal winter into four types:
24 fast-propagating, slow-propagating, standing, and jumping patterns of MJO. The model exhibits biases of overestimated
25 amplitude and faster propagation speed in the propagating MJO events. Upon further analysis, it was found that the model
26 forecasted a wetter background state. This leads to stronger forecasted convection and coupled waves, especially in the fast
27 MJO events. The overestimation of the strength and length of MJO-coupled waves results in a faster MJO mode and quicker
28 dissipation in the IAP-CAS model. These findings show that the IAP-CAS skilfully forecasts signals of MJO and its
29 propagation, and they also provide valuable guidance for improving the current MJO forecast by developing the ensemble
30 system and moisture forecast.

31 **Keywords:** MJO prediction, S2S, IAP-CAS, FGOALS-f2, Cluster Analysis

32 **1 Introduction**

33 With the increasing occurrence of metrological disasters in recent years, there has been growing attention toward S2S forecast,
34 as it bridges the gap between weather and climate forecasts and reduces disaster risks through early warnings. In November
35 2013, the WWRP/WCRP S2S prediction project (Phase 1) was launched, with the principal objectives of enhancing S2S
36 forecast accuracy and advancing our comprehension of its dynamics and climate drivers. Then, work on the S2S research
37 continued in Phase 2, from 2018 to 2023. The whole project has made a significant contribution to the development of S2S
38 prediction.

39 MJO (Madden and Julian, 1971) is a crucial predictability source of S2S forecasts. It is a significant tropical oscillation with
40 a period of 30-60 days, characterized by expansive cloud masses and precipitation systems that propagate eastward along the
41 equatorial regions. Accurate S2S prediction requires a good representation of MJO. Many studies have clarified the relationship
42 between the MJO and global weather and climate, such as monsoons (Goswami, 2012; Hsu, 2012; Lau and Chan, 1986;
43 Wheeler et al., 2009; Liu et al., 2022), tropical cyclones (Bessafi and Wheeler, 2006; Ferreira et al., 1996; Hall et al., 2001)
44 and El Niño-Southern Oscillation (ENSO; Lau et al., 2005; Zhang, 2005). The convective and circulation anomalies associated
45 with MJO establish intricate connections across global weather and climate systems on the S2S timescale. Being able to
46 accurately forecast the MJO can have a positive impact on the forecast of other related systems (Cassou, 2008; Vitart and
47 Molteni, 2010; Wu et al., 2007). Achieving an accurate forecast of MJO becomes a primary objective in the field of S2S
48 forecasts.

49 With an enhanced comprehension of the underlying physical mechanisms governing the MJO and the continuous improvement
50 of numerical models, remarkable advancements have been achieved in the MJO forecast. In Coupled Model Intercomparison
51 Project Phase 6 (CMIP6), models that exhibited lower forecast skills (Hung et al., 2013) in Coupled Model Intercomparison
52 Project Phase 5 (CMIP5) have demonstrated noteworthy improvements in the simulation of MJO (Chen et al., 2022). Generally,
53 the models in CMIP6 simulate more realistic eastward propagation and precipitation over the Maritime Continent (MC) region
54 (Ahn et al., 2019; Ahn et al., 2020).

55 However, for S2S forecasts, the improvement of model physics is one aspect of advancing S2S forecasts, as various factors
56 impact MJO forecast skills, such as initialization and ensemble generation (Kim et al., 2018). The forecast skills of the MJO
57 in most models is typically 3-4 weeks (Vitart, 2017), while the estimate of predictability of MJO is approximately 5-7 weeks
58 (Waliser et al., 2003; Neena et al., 2014). These facts underscore the persisting challenges in the S2S forecasts.

59 The realistic forecast of MJO eastward propagation is one of the challenges repeatedly mentioned in recent years (Jiang, 2017;
60 Kim, 2019; Lim et al., 2018; Wang and Lee, 2017). The MJO propagation skill is closely related to the forecast of the state in
61 the Maritime Continent (MC) region (Gonzalez and Jiang, 2017). Many studies have pointed out the "MC barrier" (Hendon
62 and Salby, 1994; Rui and Wang, 1990a; Vitart et al., 2017) during the MJO's propagation through the MC region. The "MC

63 barrier" refers to a notable deterioration of the MJO signal when it traverses the MC area, but this phenomenon is usually
64 amplified in the climate models (Kim et al., 2014b; Neena et al., 2014; Xiang et al., 2022, 2015), showing the model's limitation
65 in preserving MJO propagation within the MC region. The moisture mode theory (Raymond and Fuchs, 2009) has been
66 proposed to explain this phenomenon. It suggests that the advection of seasonal mean moisture by the MJO-related circulation
67 anomalies in the lower troposphere is crucial to MJO's propagation through the MC region (Jiang, 2017; Kim, 2019). In models
68 that are hard to capture the realistic propagation of MJO, the mean low-troposphere moisture amplitude over the MC is
69 underestimated, resulting in a weakened horizontal moisture gradient (Gonzalez and Jiang, 2017; Kim, 2017). This discrepancy
70 in moisture advection hinders MJO propagation.

71 The Institute of Atmospheric Physics at the Chinese Academy of Sciences (IAP-CAS) has been actively involved in climate
72 model development and applications since the CMIP1 in the 1990s. As for the IAP-CAS model, it has already shown a
73 significant enhancement in MJO simulation in CMIP6 compared to CMIP5 (Chen et al., 2022), but the performance of the
74 S2S system in IAP-CAS remains uncertain and requires comprehensive evaluation. Therefore, the objectives of this article are
75 fourfold: Firstly, the aim is to introduce the S2S forecast system of the IAP-CAS model. Secondly, to evaluate the forecast
76 skills of the IAP-CAS in the MJO forecast. Thirdly, the aim is to analyze the evaluation results to identify the sources of
77 forecast errors. This will facilitate further improvements in the MJO forecast. At last, we hope that the verification and analysis
78 process can provide some valuable insights for other models.

79 The structure of the paper is as follows. A thorough review of the IAP-CAS model and S2S ensemble forecast system is
80 introduced in Section 2. Section 3 describes the observation data and primary methodology utilized in the article. Section 4
81 assesses the overall MJO forecast skills in IAP-CAS. Section 5 focuses on analyzing the propagation details of the fast-
82 propagating and slow-propagating MJO. After that, in Section 6, we discuss the potential causes of any bias observed in the
83 MJO forecast. In Section 7, we summarize our findings and have a discussion.

84 **2 The global S2S ensemble forecast system of IAP-CAS**

85 The architecture of the IAP-CAS S2S ensemble forecast system is depicted in Figure 1. In this section, we will give a thorough
86 description of the S2S system, covering the model, initialization methods, ensemble generation approaches, and the resulting
87 datasets.

88 **2.1 Configuration of IAP-CAS model**

89 The climate system model CAS FGOALS-f2 (The Flexible Global Ocean-Atmosphere-Land System model Finite Volume
90 version 2, Chinese Academy of Sciences; Bao 2019; Bao et al. 2020) is the core of the IAP-CAS S2S ensemble forecast system.
91 It is developed by the State Key Laboratory of Numerical Modeling for Atmospheric Sciences and Geophysical Fluid

92 Dynamics (LASG) at the Institute of Atmospheric Physics (IAP), Chinese Academy of Sciences (CAS). We utilize the
93 institution name, IAP-CAS, as a proxy for the model.

94 FGOALS-f2 is a fully coupled model that encompasses four components: atmospheric, land, oceanic, and sea ice models, with
95 its configuration detailed in Table 1. The atmospheric component is version 2 of the Finite-volume Atmospheric Model
96 (FAMIL2; Li et al. 2019), with a standard horizontal resolution of C96, which means 96×96 grid points in each tile of the
97 cube sphere, roughly equivalent to 1-degree resolution. Vertically, it features 32 hybrid sigma-pressure levels, with the
98 uppermost level situated at 1 hPa (The Hybrid coefficients are listed in Table A1). The land surface component used in
99 FGOALS-f2 is version 4 of the Community Land Model (CLM4.0; Oleson et al. 2010; Lawrence et al. 2011), featuring a
100 horizontal resolution nearly at 1-degree resolution. The oceanic component is Parallel Ocean Program version 2 (POP2;
101 Kerbyson and Jones 2005), which utilizes a displaced-pole grid with the North Pole shifted to Greenland. This grid has a
102 resolution of gx1v6, approximately equivalent to a 1-degree horizontal resolution, and includes 60 vertical layers. The sea ice
103 component is the Los Alamos Sea Ice Model version 4.0 (CICE4; Hunke et al. 2010), sharing the exact horizontal resolution
104 as the ocean model. These four components are coupled via the coupler version 7 in the Community Earth System Model
105 (CESM; Craig et al. 2012).

106 It is worth noting that FAMIL2, the latest generation atmospheric model from LASG, has adopted the Finite-Volume Cubed-
107 Sphere Dynamical Core (FV3; Lin 2004; Putman and Lin 2007; [Harris et al., 2020](#)) as its dynamical core. FV3 solves the fully
108 compressible Euler equations on the gnomonic cubed-sphere grid and a Lagrangian vertical coordinate. [The hydrostatic solver
109 of FV3 is used in our model. Fast vertically propagating sound and gravity waves are solved by the semi-implicit method
110 \(Harris et al., 2020\).](#) This enhancement of the atmospheric component results in improved computational efficiency and
111 accuracy. Besides, the key parameterization in FAMIL2 is a Resolved Convection Precipitation scheme (RCP), which is
112 independently developed to calculate the microphysics processes in the convective precipitation for both deep and shallow
113 convection (Bao and Li, 2020). Due to the rapid phase changes occurring within the convective cloud, a sub-time step of 150
114 seconds is employed for the calculation of microphysical processes within a physical timestep of 30 minutes. FAMIL2 has
115 also implemented the University of Washington Moist Turbulence parameterization scheme (UWMT, Park and Bretherton
116 2009) as its boundary layer scheme. The microphysical parameterization used in FAMIL2 is the revised Lin scheme, which is
117 a single-moment scheme (Zhou et al., 2019).

118 **2.2 Initialization scheme of the S2S forecast system**

119 The S2S forecast system of the IAP-CAS model adopts a Newtonian nudging method with time-varying treatment (Jeuken et
120 al., 1996) to complete the initialization of the atmosphere and ocean. The reanalysis nudging and the forecast nudging are the
121 two components that make up the initialization process, which is seen in Figure 2. Table A2 provides a summary of the detailed
122 technical specifics for these two nudging processes.

123 The reanalysis nudging initializes the atmospheric variables, including temperature, surface pressure, sea level pressure, and
 124 surface wind from the NCEP Final Operational Global Analysis datasets (FNL, <http://rda.ucar.edu/datasets/ds083.2>,
 125 ds083.2|DOI: 10.5065/D6M043C6). The oceanic variable of potential temperature from the National Oceanic and Atmospheric
 126 Administration (NOAA) Optimum Interpolation Sea Surface Temperature (OISST) reanalysis data (Reynolds et al., 2007) is
 127 also included. These reanalysis data serve as observations in the eq. (1) to diminish errors in the initial condition:

$$128 \quad x(t) = x_{model}(t) + N_{rea}(t)[x_{obs}(t) - x_{model}(t)] \quad (1)$$

129 where t is the time, $x(t)$ is the field after nudging process, $x_{model}(t)$ represents the model forcing, $x_{obs}(t)$ represents the
 130 “truth” value, and $N_{rea}(t)$ is a relaxation coefficient that varies over time, which constantly adjusts the model results during
 131 the integration process, making it approximate to the observed values while being constrained by the dynamical constraints of
 132 the physical model. The calculation process for $N_{rea}(t)$ is as follows:

$$133 \quad N_{rea}(t) = \frac{\Delta t}{\frac{T}{1 + \cos(2\pi \frac{t\%T}{T})} + \Delta t} \quad (2)$$

134 Δt is the time step in FAMIL2, which is 0.5h for C96 resolution (approximately 1-degree resolution). T represents the time
 135 window with a value of 6 hours. As depicted in Figure 2a, the relaxation coefficient varies as a cosine function. It is large at
 136 the beginning and end of the temporal window, thereby facilitating accelerated convergence of the model results toward
 137 observations. While in the middle of the time window, N_{rea} becomes smaller and even drops to zero, which indicates the
 138 reliability of the reanalysis data decreases. The reason is that the reanalysis data within the time window is obtained through
 139 interpolation between its start and end values.

140 In the forecast nudging, the initialization process adheres to a similar nudging algorithm at 6-h intervals, as shown in eq. (3).

$$141 \quad x(t) = x_{model}(t) + N_{fcst}(t)[x_{fcst}(t) - x_{model}(t)] \quad (3)$$

142 Nevertheless, the atmospheric variables assimilated into the S2S system are sourced from the GFS weather forecast, denoted
 143 as $x_{fcst}(t)$. The relaxation coefficient $N_{fcst}(t)$ is as follows:

$$144 \quad N_{fcst}(t) = \frac{\Delta t}{\frac{T}{1 + \cos(2\pi \frac{t\%T}{T})} + \Delta t} \cdot \cos\left(\frac{\pi}{2} \cdot \frac{(t-t\%T)}{4mT}\right) \quad (4)$$

145 Compared to N_{rea} , N_{fcst} is multiplied by a decay factor, which also varies in accordance with the cosine function. In this
 146 context, the number of days for forecast nudging is denoted by m , and the system is configured with a 10-day forecast nudging
 147 period. Figure 2b illustrates the variation of N_{fcst} , which decreases as the reliability of weather forecast data diminishes over
 148 time, ultimately reaching zero by the 10th day.

149 In forecast nudging, we used 10 days of GFS weather forecast data for nudging. One purpose of this approach is to avoid
 150 coupling shock at initialization. Additionally, we aim to enhance the quality of initial forecasts in S2S by nudging GFS weather
 151 forecast data to ultimately improve S2S prediction accuracy, as the skill of weather forecasts is higher than that of S2S forecasts
 152 during the initial period.

153 Summarily, the S2S forecast system commences its daily forecast from the initial condition derived via reanalysis nudging. It
154 then fine-tunes the forecasts with weather prediction data through the forecast nudging process. This initialization system
155 effectively reduces system errors in the model and augments forecast accuracy.

156 **2.3 Time-lagged method for ensemble generation**

157 The value of ensemble forecasts in medium to long-term forecasts has been repeatedly emphasized (Liu, 2003; Vitart and
158 Molteni, 2009). In addition to improving the physical scheme of the model, devising an effective approach for ensemble
159 generation might have a considerable impact on the MJO forecast. The IAP-CAS S2S ensemble forecast system utilizes the
160 time-lagged method (Hoffman and Kalnay, 1983) to generate ensemble members.

161 A schematic diagram of the time-lagged method is depicted in Figure 2b. During the initial day of the forecast nudging, the
162 S2S system issues forecasts from 00Z, 06Z, 12Z, and 18Z, resulting in the generation of 4 ensemble members. The core idea
163 behind this approach is to introduce perturbations by leveraging lagged initialization times.

164 **2.4 Hindcast experiment and real-time forecast**

165 The S2S ensemble forecast system provides daily forecasts, forecasting weather and climate conditions for the upcoming 65
166 days. Out of the 65 days, 5 days are reserved for extending the ensemble members by using the time-lagged method, ensuring
167 a complete forecast for at least 60 days. Since June 1st, 2019, the IAP-CAS S2S system has been operating 16 ensemble
168 members daily for real-time forecasts. So far, approximately 8.2TB of real-time data has been uploaded to the S2S website.
169 For hindcast experiments from 1999 to 2018, the system has run 4 ensemble members daily, generating a dataset of
170 approximately 11TB. Our subsequent research is based on the 20-year hindcast experiment.

171 In 2021, the IAP-CAS model participated in phase II of the S2S Project (Vitart et al., 2017) successfully, providing the 20-
172 year hindcast and real-time forecast data generated by the S2S ensemble forecast system. Detailed information regarding the
173 data is listed in Table A3, and Table A4 shows the list of output variables. The output data is interpolated to a standardized
174 horizontal resolution of $1.5^{\circ} \times 1.5^{\circ}$, following the S2S's requirements, and is stored in version 2 of General Regularly-distributed
175 Information in Binary (GRIB2) format. The output data of the S2S system is publicly available on three S2S Data Portals
176 (ECMWF, CMA, and IRI).

177 **3 Datasets and methods**

178 **3.1 datasets**

179 The observational datasets used for the MJO verification include the NOAA daily outgoing longwave radiation (OLR;
180 Liebmann and Smith 1996), daily wind from the National Centers for Environmental Prediction (NCEP)/Department of Energy
181 (DOE) Reanalysis 2 dataset (Kanamitsu et al., 2002), daily specific humidity from ECMWF Reanalysis version 5 (ERA5;

ERA 2017), and the precipitation product from the Global Precipitation Climatology Project (GPCP; Adler et al. 2003). To facilitate computation and meaningful comparisons, both observation and hindcast datasets have been uniformly interpolated to a horizontal resolution of $2.5^\circ \times 2.5^\circ$. Seven pressure levels (1000, 925, 850, 700, 500, 300, and 200hPa) of wind and specific humidity are extracted for analysis.

3.2 MJO RMM index

To conduct a quantitative assessment of MJO, we have employed the widely used Real-time Multivariate MJO (RMM) index (Wheeler and Hendon, 2004a) to extract the MJO signal. This index consists of two components, RMM1 and RMM2, which are the first and second principal components of the combined empirical orthogonal functions (EOFs) of multiple variables, including OLR, 200hPa zonal wind (U200), and 850hPa zonal wind (U850). It serves as a tool for tracking the location and amplitude characteristics of MJO.

The calculation of the RMM index refers to the method described in Gottschalck et al. (2010). Detailed calculation steps are as follows:

- 1) Remove the 0-3 waves of the climatology and low-frequency variability of the U200, U850, and OLR variables from both the observation and hindcast data. It is noteworthy that removing low-frequency variability is to subtract the mean of the past 120 days from the anomalies. For model forecast, this is the mean model anomalies of the previous forecast days, plus the mean observed anomalies of the remaining days.
- 2) Average the anomalies between 15° S and 15° N and normalize the three variables, using the pre-computed coefficients as in Gottschalck et al. (2010).
- 3) Project the anomalies onto the observed combined EOF eigenvectors from Wheeler and Hendon (2004b) to get RMM1 and RMM2.

Bivariate anomaly correlation coefficient (ACC) and bivariate root mean square error (RMSE) are calculated using the observed and hindcast RMM indices to represent the forecast skills of the IAP-CAS model as

$$ACC(\tau) = \frac{\sum_{t=1}^N [a_1(t)b_1(t,\tau) + a_2(t)b_2(t,\tau)]}{\sqrt{\sum_{t=1}^N [a_1^2(t) + a_2^2(t)]} \sqrt{\sum_{t=1}^N [b_1^2(t,\tau) + b_2^2(t,\tau)]}}, \text{ and} \quad (5)$$

$$RMSE(\tau) = \sqrt{\frac{1}{N} \sum_{t=1}^N [(a_1(t) - b_1(t,\tau))^2 + (a_2(t) - b_2(t,\tau))^2]} \quad (6)$$

Here $a_1(t)$ and $a_2(t)$ are the observation RMM1 and RMM2 at time t ; $b_1(t)$ and $b_2(t)$ are the forecasting RMM1 and RMM2 at time t for lead τ days; N is the total number of times. It is commonly accepted that days with ACC above 0.5 are considered to have valid forecasts. Therefore, the forecast skill of a model is quantitatively defined as the maximum lead time exceeding 0.5, which approximately corresponds to the day when RMSE reaches $\sqrt{2}$.

RMM index can also be adapted to quantitatively evaluate the forecasted intensity and velocity through the calculation of the error of amplitude ($ERR_{amp}(\tau)$) and phase ($ERR_{phase}(\tau)$) as a function of lead time τ :

$$ERR_{amp}(\tau) = \frac{1}{N} \sum [AMP_b(t,\tau) - AMP_a(t)], \text{ and} \quad (7)$$

$$ERR_{phase}(\tau) = \frac{1}{N} \sum \tan^{-1} \left[\frac{a_1(t)b_2(t,\tau) - a_2(t)b_1(t,\tau)}{a_1(t)b_1(t,\tau) + a_2(t)b_2(t,\tau)} \right] \quad (8)$$

Negative (positive) $ERR_{amp}(\tau)$ indicates weaker (stronger) amplitude in forecasts. Similarly, Negative (positive)

$ERR_{phase}(\tau)$ indicates slower (faster) propagation in forecasts. Here the MJO amplitude for observation ($AMP_a(t)$) and forecast ($AMP_b(t)$) is defined as

$$AMP_a(t) = \sqrt{a_1(t)^2 + a_2(t)^2}, \text{ and} \quad (9)$$

$$AMP_b(t, \tau) = \sqrt{b_1(t, \tau)^2 + b_2(t, \tau)^2}. \quad (10)$$

3.3 Cluster analysis of MJO events

Another crucial method used in this research is cluster analysis. In Section 5, we select the representative MJO events and classify them following the work Wang et al. (2019) did. This facilitates a more focused and targeted investigation into the forecast bias of MJO in the IAP-CAS model.

An MJO event was chosen if the regional average of OLR, spanning from 10° S to 10° N and 75° E to 95° E, remained below one standard deviation for a consecutive period of 5 days during the boreal winter (November–April). Subsequently, the K-means cluster analysis is employed to categorize the chosen MJO events based on the propagation patterns from day -10 to 20 (day 0 is the day with the peak MJO in the Indian Ocean). At last, we use silhouette clustering evaluation criteria (Rousseeuw, 1987) to identify and eliminate poorly classified MJO events.

Finally, a total of 50 MJO events were selected from 1999 to 2018 winter and four types of MJO events were identified, namely the fast-propagating (10 cases), slow-propagating (16 cases), standing (12 cases), and jumping (12 cases) patterns of MJO (Fig. 5).

The fast-propagating MJO and slow-propagating MJO belong to the propagating type of MJO, characterized by their consecutive eastward propagation across the Indian Ocean to the Pacific Ocean region. On the other hand, the standing and jumping MJO represent relatively non-propagating types, where the convection remains relatively fixed or exhibits discontinuous movement. Wang et al. (2019) believe that propagating MJO events are often associated with strong and tightly coupled Kelvin waves, especially for fast-propagating MJO. This is the biggest difference between propagating MJO and non-propagating MJO.

4 Evaluation of MJO forecast skill from the IAP-CAS model

The evaluation in this section was conducted for the annual MJO events. Figure 3 demonstrates the overall MJO forecast skill in the IAP-CAS model and the improvement brought by the time-lagged ensemble method. Figure 3a shows the forecast skill of the ensemble mean is 24 days with the criterion of ACC exceeding 0.5, while the skill of individual members is about 21-22 days. Meanwhile, the ensemble mean RMSE reaches $\sqrt{2}$ at 21 days and the individual members exhibit larger RMSE,

242 reaching $\sqrt{2}$ at 16 days (Fig. 3b). The solid blue line in Figure 3b represents the ensemble spread (Leutbecher and Palmer,
243 2008) of IAP-CAS. When this ensemble spread approaches the RMSE of the ensemble mean (solid red line), it indicates that
244 the ensemble members are sufficiently dispersive. Figure 3b illustrates that the ensemble exhibits an underdispersive
245 characteristic in the early stage of the forecast. We have also observed similar issues of "underdispersive" in many other
246 models (Rashid et al., 2011; Neena et al., 2014; Kim et al., 2014b; Xiang et al., 2015), and addressing this aspect may be a
247 focal point for future model enhancements.

248 Increasing the number of ensemble members within a certain range proves effective in forecasting the uncertainty of weather
249 and climate (Hou et al. 2001). We employed the time-lagged ensemble method to further augment the ensemble members. The
250 time-lagged ensemble includes the ensemble members generated on the forecast day and from lag times. For instance, by
251 incorporating ensemble members with a lag of i ($i = 0, 1, 2, \dots$) days, the total number of members becomes $4 * (i + 1)$.
252 Upon examining the relationship between lag i days and forecast skill, it was found that the skill increases as i increases at
253 first, but then it reaches a plateau when $i > 3$ (see Fig. A2). This suggests that the forecast skill of the 16 members may
254 represent the limit of the time-lagged ensemble method in IAP-CAS. Figure 3d shows the ensemble of 16 members is more
255 dispersive than 4 members, which is illustrated by less distinction between RMSE and Spread in the 16-member system. The
256 ensemble mean of 16 members achieves a skill of 26 days, surpassing the skill of 4 members by two days (Fig. 3c).

257 Numerous prior investigations have demonstrated that MJO forecast skill is sensitive to the MJO amplitude in many models
258 (Lin et al., 2008; Rashid et al., 2011; Wang et al., 2014; Xiang et al., 2022), and this characteristic is also evident in the IAP-
259 CAS model. We classify an MJO case as an initial (target) strong case if its initial (target) amplitude is greater than 1, while
260 an event with an initial (target) amplitude less than 1 is classified as an initial (target) weak case. Figures 4a-b show that in the
261 IAP-CAS model, the forecast skills of strong MJO cases are generally higher than weak cases, especially in the target strong
262 (weak) cases.

263 The amplitude and phase of MJO serve as additional indicators for a detailed assessment of MJO forecast performance. For
264 initially strong MJO cases, we analyze the MJO amplitude and forecasted phase angle error (Figs. 4b-c). The individual
265 member has a stronger amplitude than observation, which leads to a relatively strong amplitude in the ensemble mean during
266 the initial 40 days. However, as the noise rapidly increases, the phase error of the individual members also escalates (as shown
267 in Fig. 4c). The phase error results in a mutual cancellation in positive and negative phases of MJO among ensemble members,
268 leading to a rapid weakening of the amplitude in the ensemble mean. In Figure 4d, the phase error of the ensemble mean
269 indicates that the speed of forecasted MJO tends to decrease at first and then start increasing around the 10th day. A more
270 detailed investigation into the speed of propagating MJO events will be described in Section 5.

271 **5 The forecast of MJO propagation**

272 We present a qualitative diagnostic of a 20-year hindcast experiment to evaluate the overall forecast skills of IAP-CAS in
273 Section 4. This analysis provides us with preliminary insights into the performance and biases of the system. Given that the
274 MJO is more pronounced during boreal winter, our focus is concentrated from November to the following April. Based on
275 Wang et al. (2019), we aim to conduct further investigations into different types of boreal winter MJO events to explore the
276 physical explanation of system biases.

277 In Section 3, we have already described the methodology for classifying MJO events and results. Figure 5 compares the
278 composited propagation patterns of precipitation and U850 between observation and forecast for four different MJO types. In
279 observations, the fast-propagating (Fig. 5a) and slow-propagating (Fig. 5b) MJO exhibit a consecutive eastward propagation
280 structure from the Indian Ocean across the MC region to the Pacific Ocean. The primary distinction between the two types lies
281 in their propagation speed. The fast-propagating MJO demonstrates a faster speed, with a velocity of 4.58 m/s, compared to
282 the slow-propagating type, which moves at 4 m/s. The standing MJO (Fig. 5c) remains relatively stationary over the Indian
283 Ocean and does not continue to propagate eastward. The jumping MJO (Fig. 5d) shows a convective system that bypasses the
284 MC region and directly jumps from the Indian Ocean to the Pacific Ocean. Here, fast MJO and slow MJO are considered
285 propagating MJO events, while the latter two types are regarded as non-propagating MJO events.

286 The observed U850 displays a coupled structure characterized by equatorial westerly anomalies of the Kelvin wave component
287 located west of the convection, and easterly anomalies of the Rossby wave component located east of the convection (Rui and
288 Wang, 1990b; Adames and Wallace, 2014; Wang and Lee, 2017). As illustrated in Figure 5, a distinct contrast between
289 propagating MJO and non-propagating MJO can be found in the circulation at the low level: in the propagating MJO events,
290 the Kelvin wave response is strong and tightly coupled with the center of convection, which is shown in the stronger and
291 eastward-extending easterly wind component, particularly prominent in fast MJO events. Many previous studies (Benedict
292 and Randall, 2007; Hsu and Li, 2012; Wang and Lee, 2017) have also indicated that the presence of low-level easterly winds
293 is a key signal that contributes to the eastward propagation of MJO by inducing low-level convergence and premoistening to
294 the east of the major convection. In the non-propagating MJO events, the easterly wind is weak and tends to decouple from
295 the major convection.

296 The model accurately reproduces the propagating morphology of the MJO and exhibits coupled signals of Kelvin and Rossby
297 waves (Figs 5e and 5f). However, a noticeable acceleration in speed is evident, particularly in the case of fast MJO, reaching
298 speeds of 6 m/s, while the simulated slow MJO moves at 5 m/s. Figure 5g also shows that the forecast for standing MJO
299 remains somewhat imprecise. This aspect is also evident in the MJO forecast skill depicted in Figure 6, where the standing
300 MJO has the lowest skill (13 days). For each MJO type, we consider the skill as the ACC of the cases initiated from day -20

301 to day 15 (Xiang et al., 2015). Figure 6 displays that the fast MJO achieves the highest skill at 32 days, while the jumping MJO
302 and slow MJO exhibit skills of 23 and 21 days, respectively.

303 Additionally, from the Hovmöller diagram of observed propagating MJO (Figs. 5a and 5b), a significant change in convection
304 is observed after crossing the MC region, which is marked by a decrease in intensity and a slower propagation speed. This
305 change is roughly delineated by the 135° E, which is commonly referred to as the “MC barrier”. As mentioned above, the “MC
306 barrier” effect is usually amplified in the climate models. In the IAP-CAS model, the forecasted convective signal of slow
307 MJO appears to halt after crossing the MC region. Could this indicate an amplification of the "MC barrier" issue in the IAP-
308 CAS model? However, this phenomenon is less pronounced in the simulation of fast MJO. Due to the zonal averaging in the
309 Hovmöller diagram, some information may be obscured. Further investigation is required to determine the detailed
310 characteristics of the propagating MJO simulated by the model.

311 Figure 7 presents the evolution patterns of propagating MJO. In the first 10 days, it is noticeable that the forecasted precipitation
312 intensity of propagating MJO is significantly higher than observed, especially in the case of fast MJO. Coupled winds in 850
313 hPa also exhibit stronger magnitudes, with a larger zonal scale. The forecasted location of the major convection is relatively
314 biased towards the east, which further confirms that there is an overestimation of the propagation speed. On the 15th day, the
315 MJO convective system crosses the MC region and reaches the eastern Pacific. It is worth noting that the forecasted negative
316 phase of MJO exhibits a significant development, with an accelerated speed, gradually intruding into the positive phase (Figs.
317 7b and 7d). By the 20th day, the development of the negative phase has further intensified, extending its influence into the
318 tropical eastern Pacific region, while in the observation, the negative phase remains east of the MC region. In the later stages,
319 as the negative phase intrudes, the forecasted convective signal in the positive phase is almost absent due to the inherently
320 weaker convection in slow MJO. The disappearance of the slow MJO signal observed in the Hovmöller diagram after crossing
321 the MC region may stem from the intrusion of the negative phase. This might differ from the commonly defined issue of "MC
322 barrier" amplification observed in many models.

323 In Figure A3, simulations show that both standing and Jumping MJO also exhibit overall enhanced convective intensity.
324 However, they accurately capture the non-propagating characteristics of the observed MJO, such as the weak coupling of
325 Kelvin waves and the strong coupling of Rossby waves.

326 **6 The possible physical explanation for the forecast biases**

327 Section 5 highlights some biases observed in the forecast of propagating MJO, which includes stronger amplitude and faster
328 propagation speed in the IAP-CAS model. These biases are also mentioned in Section 4. In this section, we aim to unravel the
329 physical mechanisms underlying these biases.

330 As a large-scale convective system, MJO's genesis, evolution, and dissipation are intricately linked to atmospheric moisture
 331 (Wang, 1988; Kemball-Cook and Weare, 2001; Maloney, 2002; Wang and Lee, 2017). Given that the model forecasts exhibit
 332 a systematic bias of stronger amplitude, we start with the diagnosis of the background state in moisture. Figure 8 shows the
 333 winter mean specific humidity averaged over 10° S–10° N. A clear positive bias of the background moisture state in the IAP-
 334 CAS model is observed (Fig. 8c), which can enhance the convection in the MJO. However, the distribution of this moisture
 335 bias is non-uniform. Figure 8c illustrates that the positive moisture bias is more pronounced towards the western Indian Ocean
 336 and the central-eastern Pacific, and this bias gradually spreads to the upper levels. However, in the MC region, the positive
 337 moisture bias is smaller and primarily concentrated in the low level. We speculate that higher evaporation fluxes in the model
 338 may be the reason for the positive moisture bias. Therefore, the reduction in oceanic surface area within the MC region
 339 contributes to a decrease in this positive bias.

340 Figure 9 displays the precipitation-induced condensational heating (Q_2) during fast MJO and slow MJO events. The
 341 condensational heating serves as a proxy for the distribution of convection, which was estimated by the moisture sink defined
 342 as

$$343 \quad Q_2 = -L_v \left(\frac{\partial q}{\partial t} + \vec{V} \cdot \nabla q + \omega \frac{\partial q}{\partial p} \right), \quad (11)$$

344 where q is the specific humidity, \vec{V} is the horizontal circulation, ω is vertical pressure velocity, and L_v is the latent heat
 345 at condensation, which is a constant here. The vertical distribution of Q_2 reveals that both fast MJO and slow MJO events in
 346 the model forecasts trigger stronger convection, particularly in the fast MJO events. Furthermore, the enhanced convective
 347 heating leads to a strong response in the coupled MJO-related circulation (Fig. 9). From the 1st day to the 10th day, there is a
 348 gradual strengthening process observed in the simulated convection, particularly pronounced in fast MJO, with its intensity
 349 peaking on the tenth day.

350 To further understand the propagation and intensity variations of MJO in the IAP-CAS model, it is necessary to comprehend
 351 the underlying physical processes associated with it. Under the framework of “moisture mode”, Jiang (2017) performed a
 352 moisture budget analysis on the latest generation of general circulation models (GCMs) and identified the key processes for
 353 the eastward propagation of MJO. This research revealed that the advection ($\vec{V}' \cdot \nabla \bar{Q}$) of the seasonal mean moisture (\bar{Q}) by
 354 the MJO anomalous circulations (\vec{V}') plays a crucial role in the propagation of MJO. By increasing moisture eastward and
 355 decreasing it westward of the MJO convection, the advection regulates the propagation. (Kim et al., 2014a; Adames and Kim,
 356 2016; Jiang et al., 2018). Among the two determining factors (\vec{V}' and \bar{Q}), the role of the moisture gradient term is further
 357 emphasized. Many studies (Gonzalez and Jiang, 2017; DeMott et al., 2018; Ahn et al., 2020) have demonstrated that the mean
 358 moisture's horizontal gradient plays a crucial role in determining the propagation of MJO (Fig. 10a). It is well-forecasted in
 359 the models that simulate MJO well, leading to realistic horizontal mean moisture gradients and, thus, well-forecasted horizontal
 360 moisture advection associated with the MJO (Hsu and Li, 2012; Kim et al., 2014a; Nasuno et al., 2015; Adames and Wallace,

361 2015; Gonzalez and Jiang, 2017). The IAP-CAS model is capable of reproducing this gradient, although there is an overall
362 stronger moisture bias (Fig. 10b). Here, the \bar{Q} presented is the winter mean specific humidity at 850 hPa (\bar{Q}_{850}). Research has
363 indicated that the \bar{Q}_{850} is representative (Kim, 2019), and subsequent analysis also focuses on the 850 hPa level.

364 Figure 11 shows the composite equatorial U850 anomalies averaged over the 15° S-15° N for fast MJO and slow MJO
365 respectively. It depicts the transition from westerly to easterly winds in the MC region (as enclosed by the two blue dashed
366 lines), leading to the change from positive advection to negative advection. On the 1st and 5th days, the MC region is
367 predominantly occupied by easterly winds, while from the 10th to the 20th day, the region is primarily characterized by westerly
368 winds in both fast MJO and slow MJO. However, the forecasted amplitude of low-level wind is significantly stronger, which
369 can be caused by the enhanced MJO convection as explained earlier.

370 The MJO anomalous circulation patterns in the MC region result in a positive moisture advection on the eastern part of the
371 MJO during the early stages of MJO's development, which facilitates the propagation of convection in the positive phase. We
372 refer to this process as the "developing phase". Figure 12 provides a detailed illustration of this process. Conversely, during
373 the later stages, there is a negative moisture advection on the western side of the MJO, which leads to the propagation of
374 convection in the negative phase and promotes the dissipation of the MJO. We refer to this process as the "decaying phase"
375 (Fig. 12). Compared to the observation, the stronger amplitude of the low-level moisture advection ($\bar{\mathbf{V}}' \cdot \nabla \bar{Q}$) in the model
376 explains the gradual enhancement of convective moist phases during the early stages and the amplification of convective dry
377 phases during the later stages (Fig. 13). The model's moist environment leads to intensified convection, triggering the
378 strengthening of coupled wind fields, which in turn enhances the moist phase in the early stage and the dry phase in the later
379 stage of convection. Consequently, during the development phase of the MJO, its amplitude gradually strengthens. Conversely,
380 during the decaying phase of the MJO, the intensity of the dry phase also progressively increases.

381 As the simulated propagating MJO gradually intensifies, we observe an enhancement of easterly winds on the east of the
382 convective center, accompanied by an overestimation in zonal scale, indicating the triggering of stronger Kelvin waves (Figs
383 7b and 7d). According to Wang et al. (2019), MJO with a larger zonal scale will experience an increased eastward propagation
384 speed since the phase speed is inversely proportional to the wave number. This phenomenon is also observed in observation,
385 where the Kelvin wave response to fast MJO exhibits a larger zonal scale compared to slow MJO. Subsequently, during the
386 decay phase of the propagating MJO, the model exhibits a pronounced Rossby wave response triggered by the MJO, leading
387 to the intrusion of convective negative phases and facilitating the dissipation of the MJO.

388 In addition to examine the winter mean moisture state (\bar{Q}), we have analyzed MJO-related moisture anomalies (Q') as well
389 (Fig. 14). By comparing the evolution pattern of moisture anomalies between slow MJO and fast MJO, it is found that the
390 moisture anomalies in the eastern part of fast MJO are more intense compared to the slow MJO. This results in stronger low-
391 level moisture transport towards the convective region, thereby also facilitating the intensification and acceleration of the MJO.
392 Moreover, there is a significant distinction in the spatial correlation between fast and slow MJO and it happens as early as the

393 1st day. As the forecast lead time progresses, the accuracy of the moisture forecast deteriorates, while fast MJO events display
394 comparatively better performance. The disparity in moisture anomalies is possibly a pivotal factor contributing to differences
395 in forecast skills between the fast (32 days) and the slow MJO (21 days). This underscores the significance of improving
396 moisture forecast in the MJO forecast.

397 **7 Summary and discussion**

398 **7.1 Summary**

399 The graphical abstract presents a workflow for this paper, outlining the structure of this work. This study introduces a newly
400 developed S2S ensemble forecast system of the IAP-CAS model. The introduction primarily focuses on the numerical model,
401 initialization, ensemble generation, and post-processing aspects of the S2S system. Then we aim to identify potential
402 possibilities for developing this S2S system through a comprehensive assessment of its forecast skills. Based on the 20-year
403 hindcast experiment, the IAP-CAS model shows comparable skill (24 days) to other S2S models. However, the ensemble
404 forecast for MJO has been demonstrated to be underdispersive. A detailed examination of the propagating MJO forecasted in
405 the IAP-CAS model reveals that the amplitude of the convection is overestimated with an increasing propagation speed,
406 particularly in the fast MJO events. These biases are accompanied by a faster dissipation of the MJO.

407 The root cause of these biases lies in the model's wetter environment, which leads to enhanced convection and strengthened
408 circulation coupled with convection. This, in turn, further amplifies convection during the development of propagating MJO.
409 The gradual intensification of MJO strength and coupled Kelvin waves is mainly associated with the stronger amplitude of the
410 low-level moisture advection ($\vec{V}' \cdot \nabla \bar{Q}$) in the forecast. The overestimate in the zonal scale of Kelvin waves accelerates the
411 propagation of the propagating MJO in the model. Similarly, the strengthening of Rossby waves also hastens the dissipation
412 of the MJO. Moreover, the differences in forecast skills between the fast MJO and the slow MJO may be attributed to
413 discrepancies in moisture anomalies (Q') forecast. This further underscores the significance of accurate moisture forecasts.

414 **7.2 Discussion**

415 In Figure A4, we compare the forecast skill of the IAP-CAS model with 11 other S2S models. The MJO index of 12 S2S
416 models and ERA-Interim from the S2S website (<http://www.s2sprediction.net/>) is used for evaluation during the standard
417 hindcast period 2001-2010. In Figure A4, we observe improved forecast skill in ensemble forecasts compared to deterministic
418 forecasts. Among the 12 S2S models, the IAP-CAS model exhibits MJO skill above the mean skill level, while the ECMWF
419 model stands out as the highest-performing model. Figure A5a shows that the skill of individual members in ECMWF is
420 approximately 17-18 days, whereas the ensemble mean demonstrates an extended skill of up to 30 days. This phenomenon
421 may be attributed to the ECMWF model's considerable dispersion (Fig. A5b), which once again underscores the critical role
422 of ensemble dispersion in forecasting uncertainties of weather and climate.

423 Therefore, the forthcoming phase in our model's development plan encompasses increasing model dispersion through
424 improved ensemble perturbation methods, with the ultimate goal of improving model forecast skills. The method of orthogonal
425 conditional nonlinear optimal perturbations (CNOPs, Mu et al. 2003) and the second-order exact sampling (Pham, 2001) are
426 both promising approaches for generating initial perturbations in the model. This method allows the generation of a set of
427 initial perturbations in different orthogonal perturbation subspaces, each with the maximum potential for nonlinear
428 development. When applied to ensemble forecast using a simple Lorenz-96 model, the CNOPs method has demonstrated
429 higher forecast skill compared to the commonly used linear Singular Vectors (SVs) method (Lorenz, 1996). Furthermore,
430 PDAF (Parallel Data Assimilation Framework, Nerger et al., 2020) provides an efficient method known as second-order exact
431 sampling, which uses the long-time variability of the model dynamics to estimate the uncertainty. Evidence has already
432 suggested that the use of second-order exact sampling can greatly improve the skill in sea ice extent throughout the Arctic and
433 along the Northern Sea Route (Yang et al., 2020). We plan to explore the application of CNOPs and second-order exact
434 sampling in the IAP-CAS model in the future and eagerly anticipate the potentially significant results it may yield. Additionally,
435 using machine learning to improve the skill of ensemble forecast is also a viable way to enhance the ensemble forecast of our
436 model.

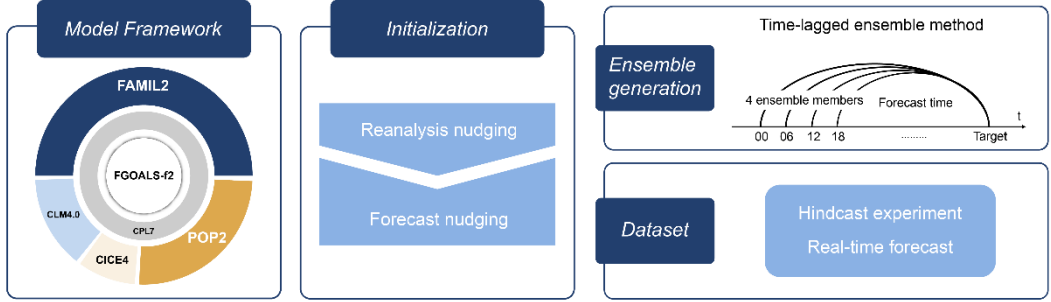
437 In addition to exploring ensemble perturbations, we also intend to enhance the initialization system of the model. Recognizing
438 the moisture is crucial in the forecast of MJO and acknowledging the issue of moisture bias in the IAP-CAS model, it is
439 essential to take measures to ameliorate moisture forecast in our model. The recent research by Zeng (Zeng et al., 2023)
440 provides convincing evidence that humidity initialization can indeed significantly enhance MJO forecast in the IAP-CAS S2S
441 forecast system, especially in the 2 and 3 phase of MJO propagation. However, it is worth noting that changes in the mean
442 state have a significant impact on MJO development (Hannah et al., 2015; Kim, 2019), we must pay attention to the influence
443 of moisture initialization on the mean state. Moreover, the current S2S system's initialization process uses the nudging method,
444 and it is worthwhile to explore more efficient methods to enhance the initialization process.

445 We are also considering increasing the resolution of the model to C384 (25 km) globally. A High-resolution coupled model
446 could better represent the MJO (Crueger et al., 2013). This improvement could be attributed to the enhanced resolution, which
447 better captures the ocean-atmosphere interaction – a critical factor for MJO convection. Increasing the resolution is also
448 meaningful for enhancing forecasts in the MC region by accurately depicting terrain distortion (Hsu and Lee, 2005; Inness and
449 Slingo, 2006; Wu and Hsu, 2009). Further optimizing the model's physical processes and dynamic-physical coupling is also
450 believed to enhance the forecast of the MJO (Zhou and Harris, 2022). As the foreseeable resolution and complexity of the
451 model increase in the future, the issue of power consumption on X86 architecture processors for handling the growing amount
452 of data will become more pronounced. We have plans to port the model to the computing platform based on ARM architecture
453 to address the challenges posed by the explosive growth of data.

Component	Model name	Horizontal Resolution	Vertical levels	Reference
Atmosphere	FAMIL2	Cubed Sphere Grid (C96, $\sim 1^\circ \times 1^\circ$)	32 in the hybrid levels	Li et al. 2019
Land	CLM4.0	Nested subgrid hierarchy (f09, $\sim 1^\circ \times 1^\circ$)	15 soil levels and 3 snow levels	Oleson et al. 2010; Lawrence et al. 2011
Ocean	POP2	Displaced-pole grid (gx1v6, $\sim 1^\circ \times 1^\circ$)	60 levels	Kerbyson and Jones 2005
Sea ice	CICE4	Displaced-pole grid (gx1v6, $\sim 1^\circ \times 1^\circ$)	5 levels	Hunke et al. 2010

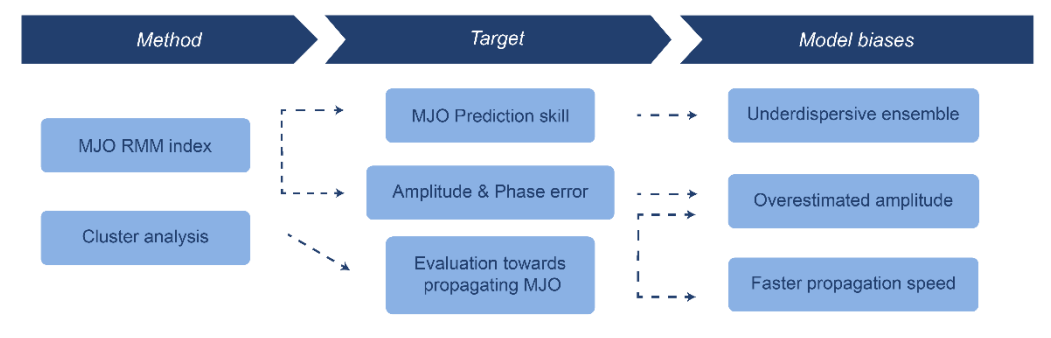
1 An overview of IAP-CAS S2S ensemble forecast system

EXPECTED: Readers can acquire a thorough and organized comprehension of this system



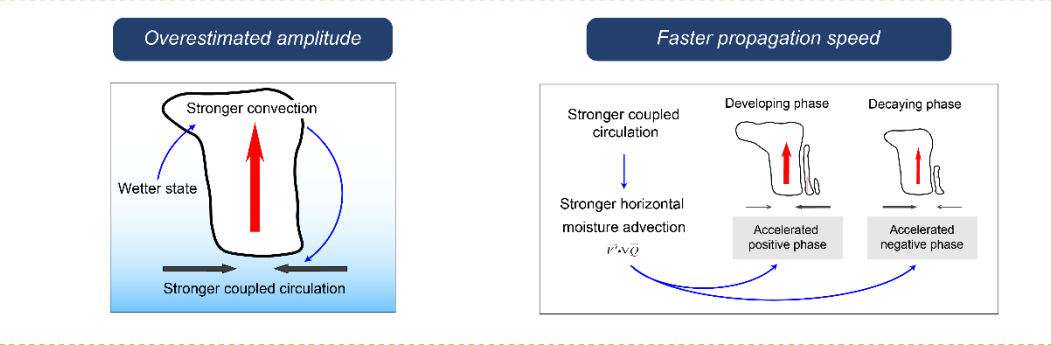
2 Evaluation of MJO forecast in IAP-CAS S2S system

EXPECTED: Gain insights into the S2S system's performance in S2S forecast



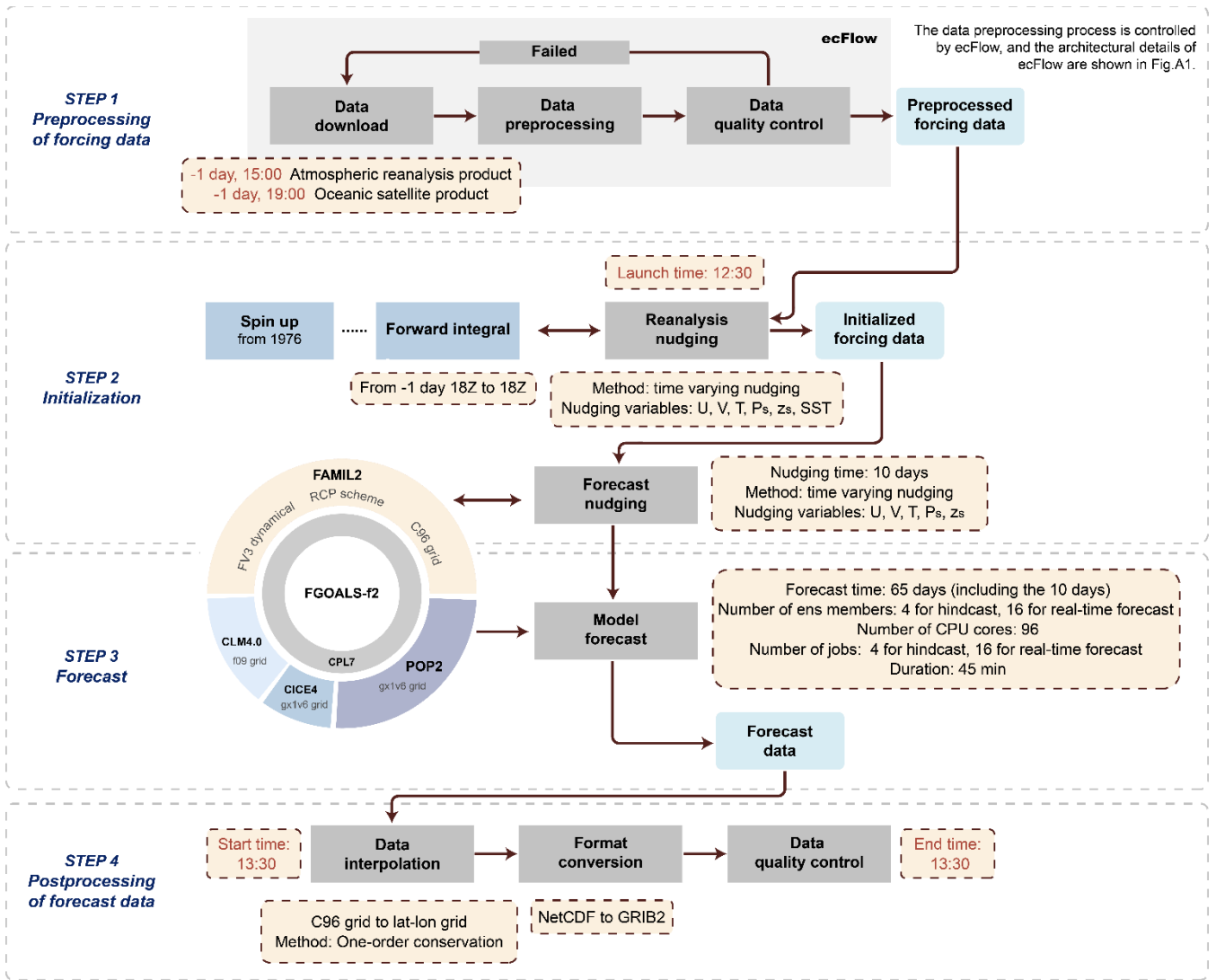
3 The possible explanation about the prediction biases

EXPECTED: Identify the sources of system errors for further improvements



455
456

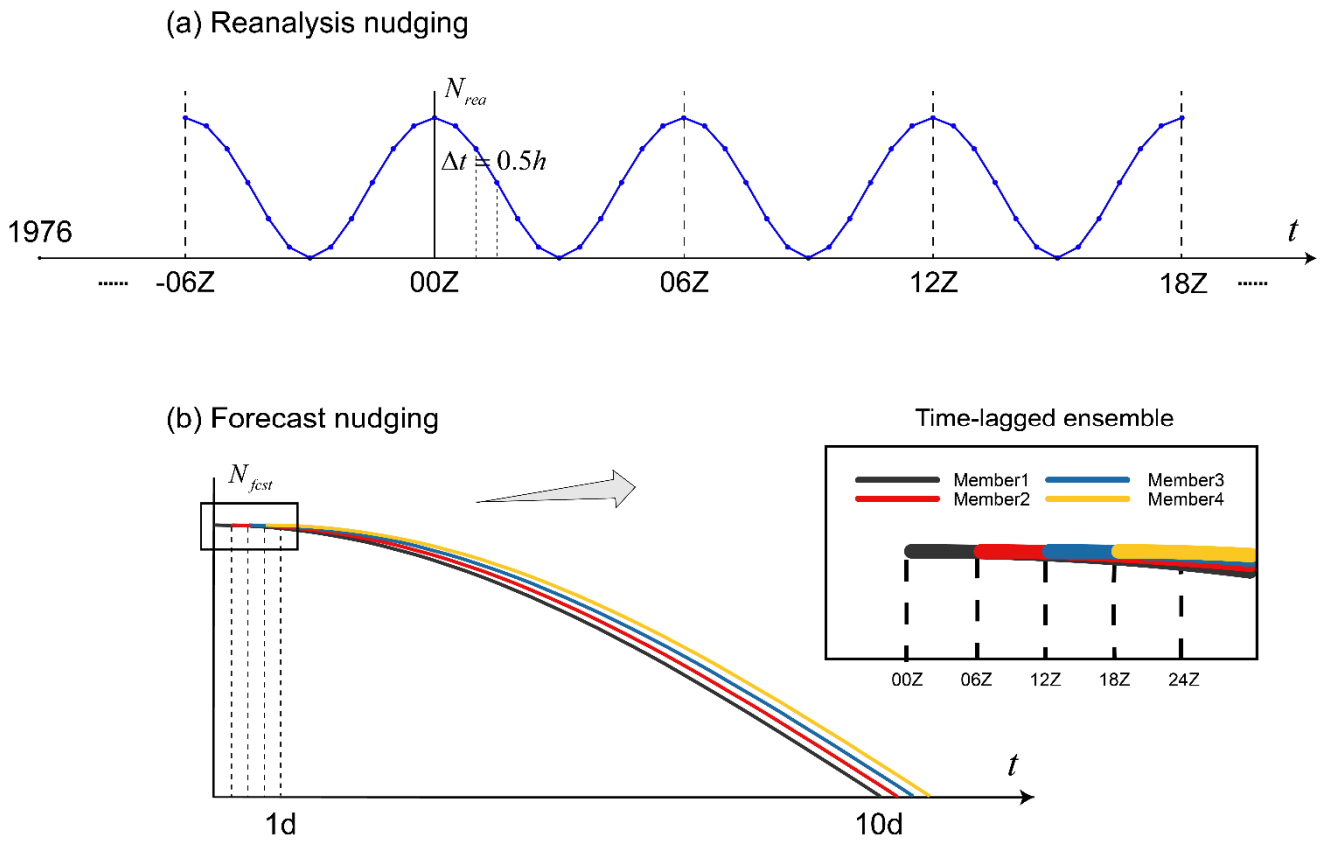
The graphical abstract



457
458

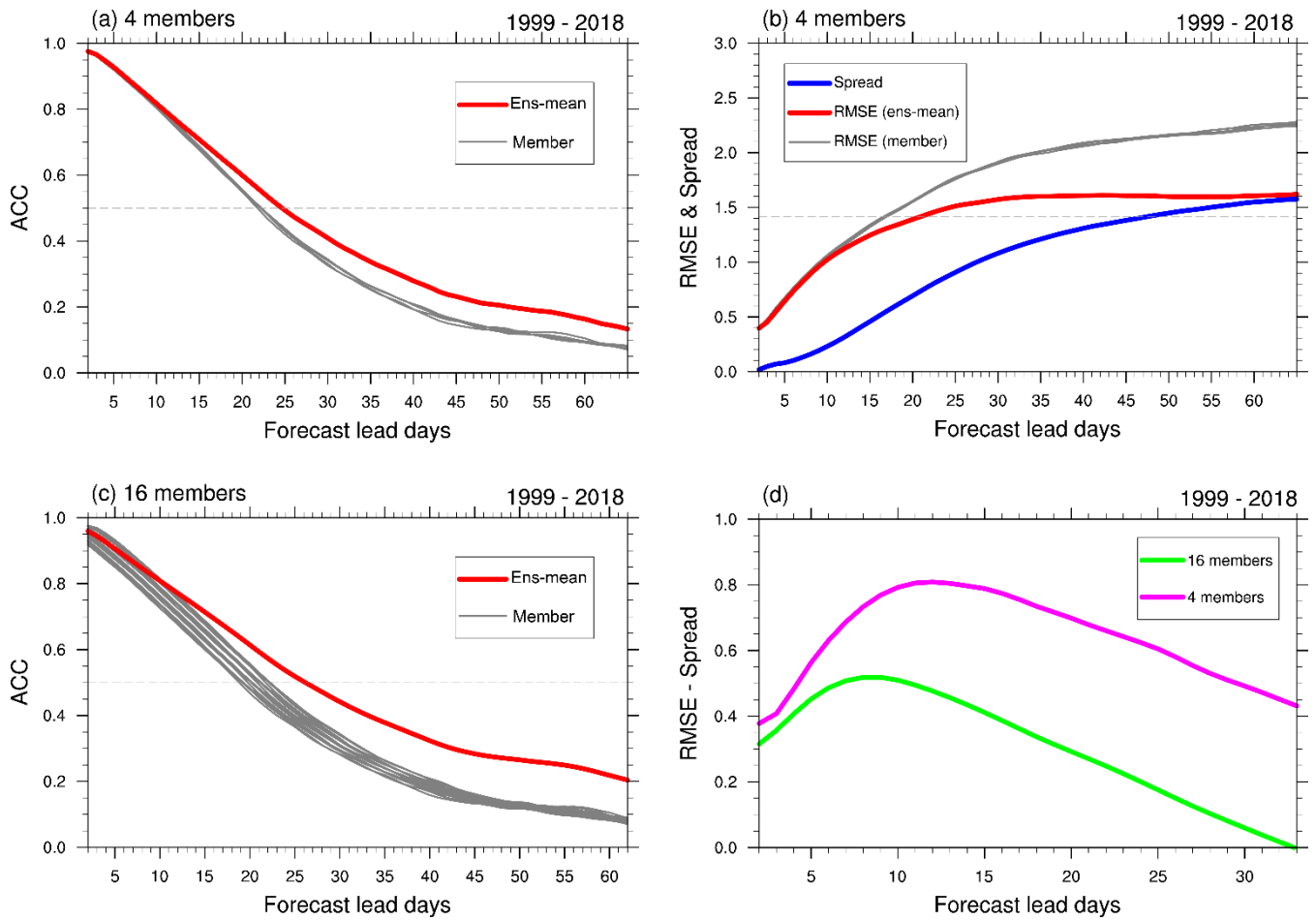
The time marked in red here is local time (beijing time)

Figure 1. The structure of the IAP-CAS S2S ensemble forecast system



459

460 **Figure 2. The initialization scheme of the S2S ensemble forecast system in the IAP-CAS model. The relaxation coefficient (N) as a**
 461 **function of time (t) in (a) the reanalysis nudging and (b) the forecast nudging. In (a), The reanalysis nudging begins on January 1,**
 462 **1976. The dots indicate the nudging process every 30 minutes. In (b), the solid lines of 4 colors represent the 4 ensemble members**
 463 **with their generation facilitated through the application of the time-lagged method.**



464

465

466

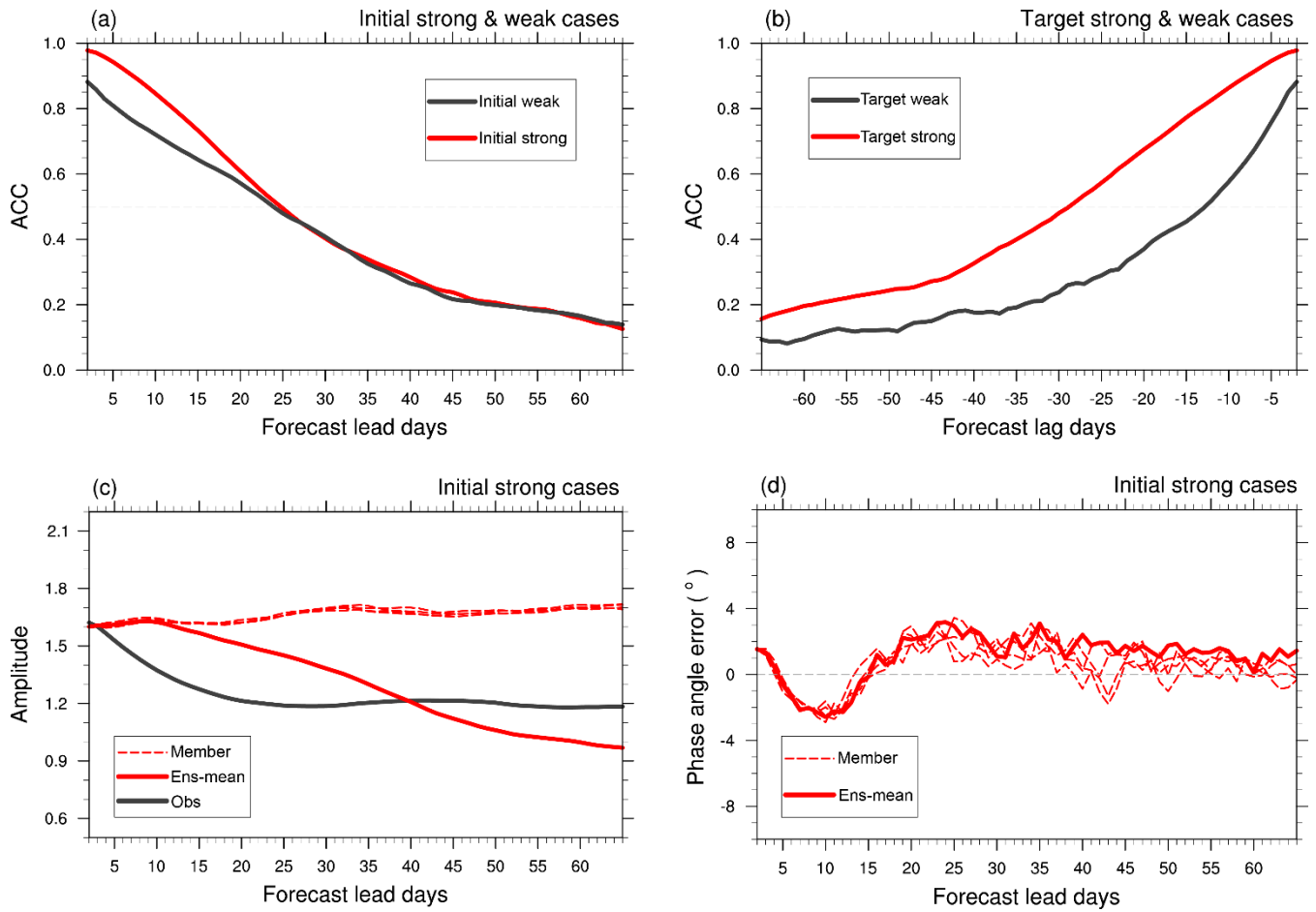
467

468

469

470

Figure 3. MJO forecast skill of IAP-CAS for the annual MJO events over 20 years (1999-2018) re-forecast data. (a) The bivariate anomalous correlation coefficient (ACC) and (b) The Root Mean Squared Error (RMSE) varied with forecast lead days for individual members (gray solid line) and ensemble mean (red solid line). The blue solid line denotes the ensemble spread. (c) The ACC of individual members and ensemble mean, as generated by the time-lag method resulting in 16 ensemble members. The dashed line in (a) and (c) has the values of 0.5, and it represents 1.414 in (b). (d) The difference between RMSE and Spread of 4-member ensemble mean (purple solid line) and 16-member ensemble mean (green solid line).



471

472

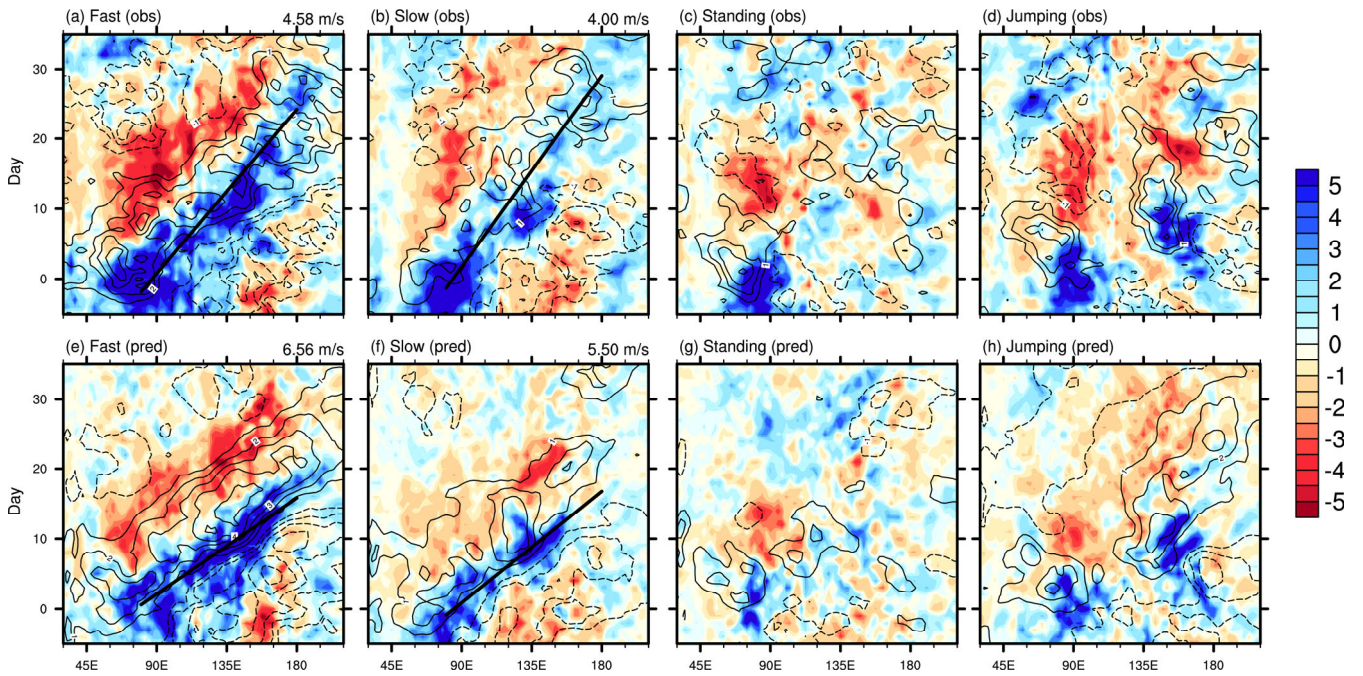
473

474

475

476

Figure 4. The ACC (a) varied with forecast lead days for initially strong (red) and weak (black) cases and (b) varied with forecast lag days for target strong (red) and weak (black) cases from the ensemble mean. The dashed lines in (a) and (b) have the values of 0.5. (c) The forecast of MJO amplitude varied with forecast lead days for initially strong cases from observation (black solid line), individual ensemble members of the model (red dashed line) and their ensemble mean (red solid line). (d) The forecast of MJO phase angle error (°) for initially strong cases (black solid line). The dashed line in (d) is the reference line with the values of 0.



477

478

479

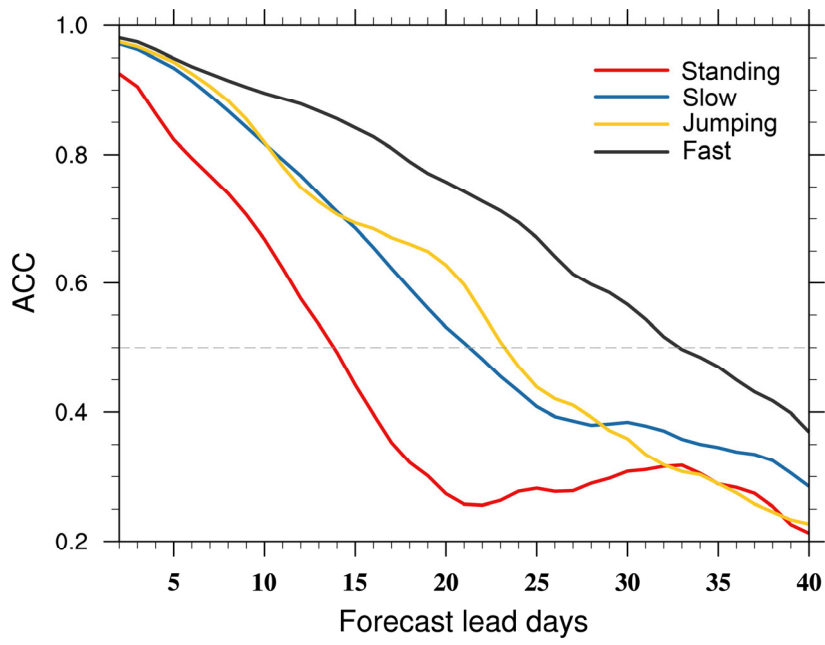
480

481

482

483

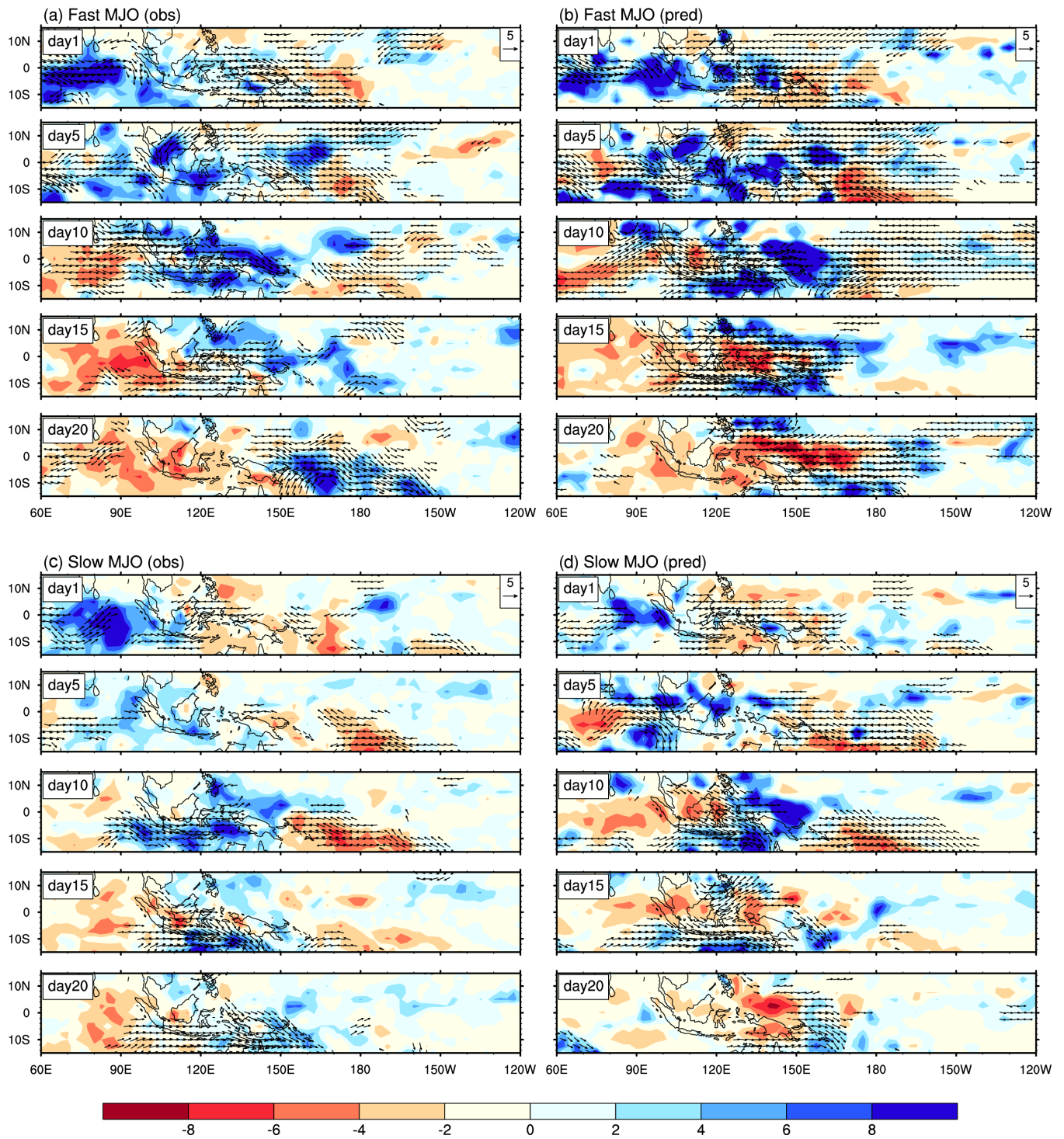
Figure 5. 10°S – 10°N averaged Precipitation anomalies (shading; mm day^{-1}) and 850-hPa zonal winds anomalies (contours with an interval of 1 m s^{-1}) varied with longitude (x-axis) and time lag (y-axis; days) composited for four types of the boreal winter MJO. The top row is for observation (NCEP winds and GPCP precipitation), and the bottom row is for model forecasts. The thin solid black lines represent positive values and the dashed lines represent negative values. The thick solid black line represents the propagation trajectory of the MJO, derived via least squares regression. The propagation speed of the propagating MJO is annotated in the top right corner of the panels.



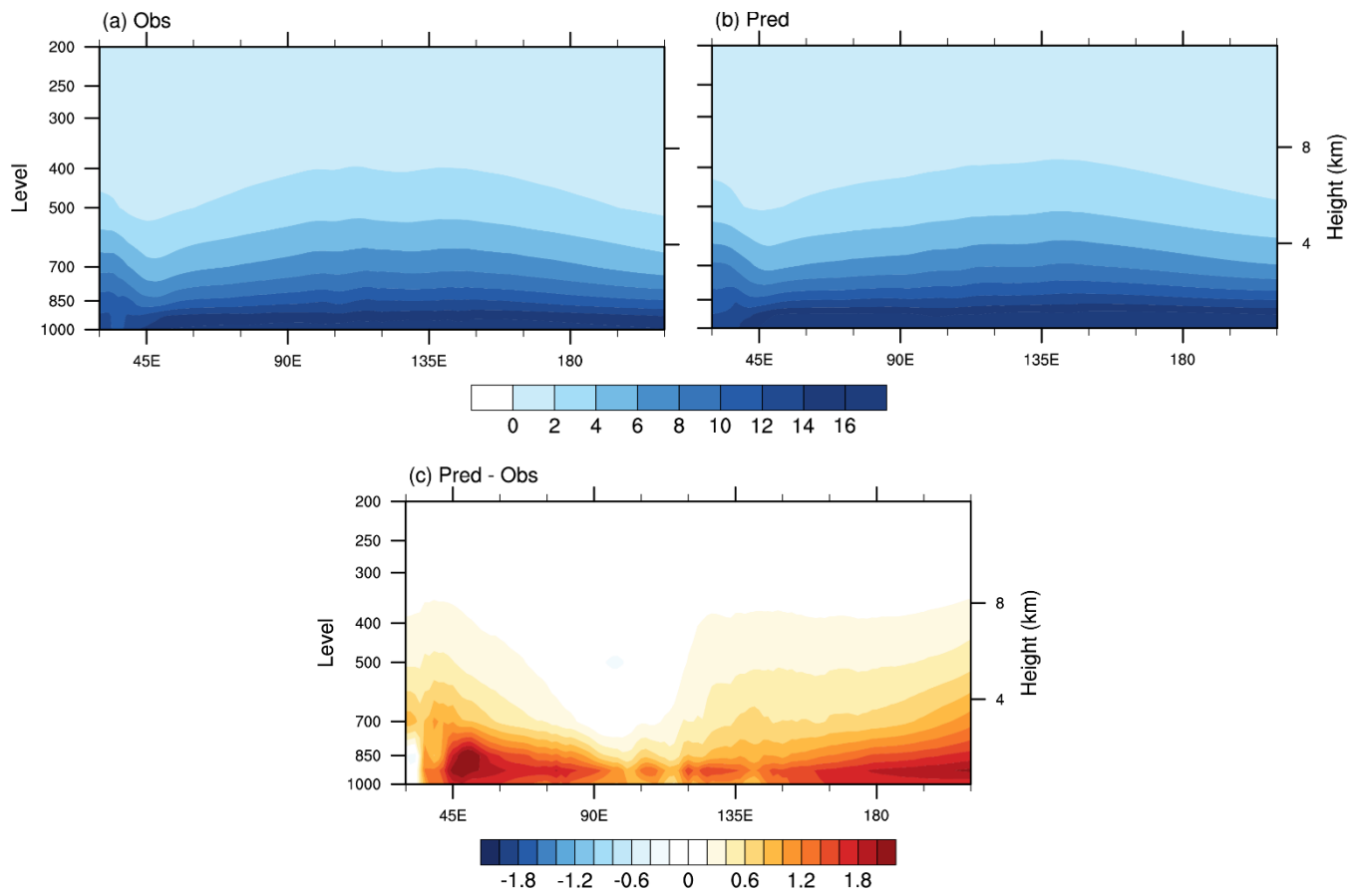
484

485 **Figure 6. The bivariate ACC as a function of forecast lead days for fast, slow, jumping, and standing MJO events. The dashed line**
 486 **has a value of 0.5.**

487



488
 489 **Figure 7. Evolution patterns of the composite precipitation (shading; mm day⁻¹) and 850-hPa winds (vectors; m s⁻¹) anomalies**
 490 **(exceeding 2 m/s) for day 1, day 5, day10, day15 and day 20 in (a) observed fast MJO, (b) simulated fast MJO, (c) observed slow**
 491 **MJO and (d) simulated slow MJO.**

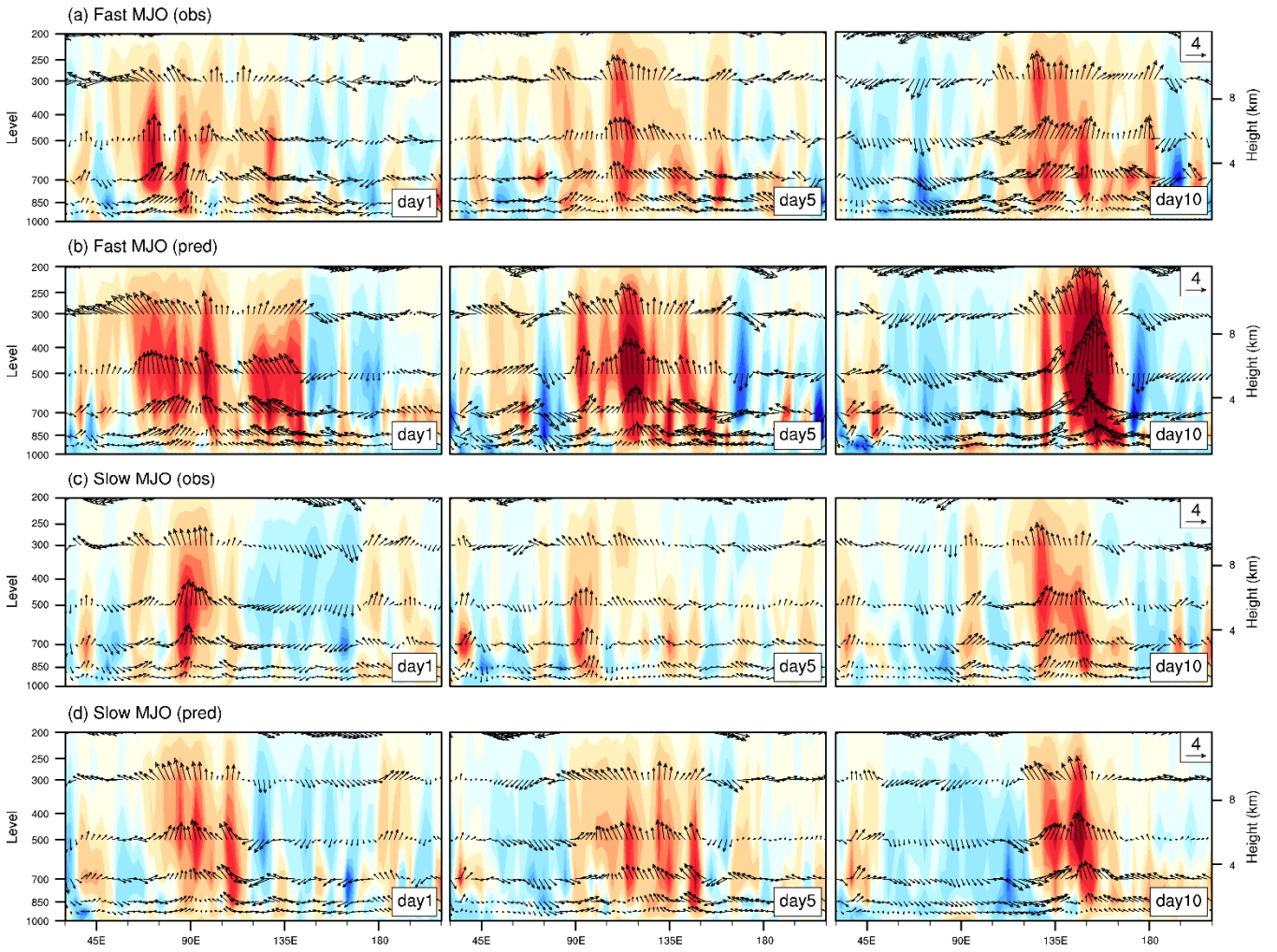


492

493

494

Figure 8. The longitude-vertical profiles of winter (November–April) mean specific humidity (g kg^{-1}) averaged over 10°S – 10°N for (a) observation, (b) IAP-CAS model, and (c) the difference between IAP-CAS model and observation.



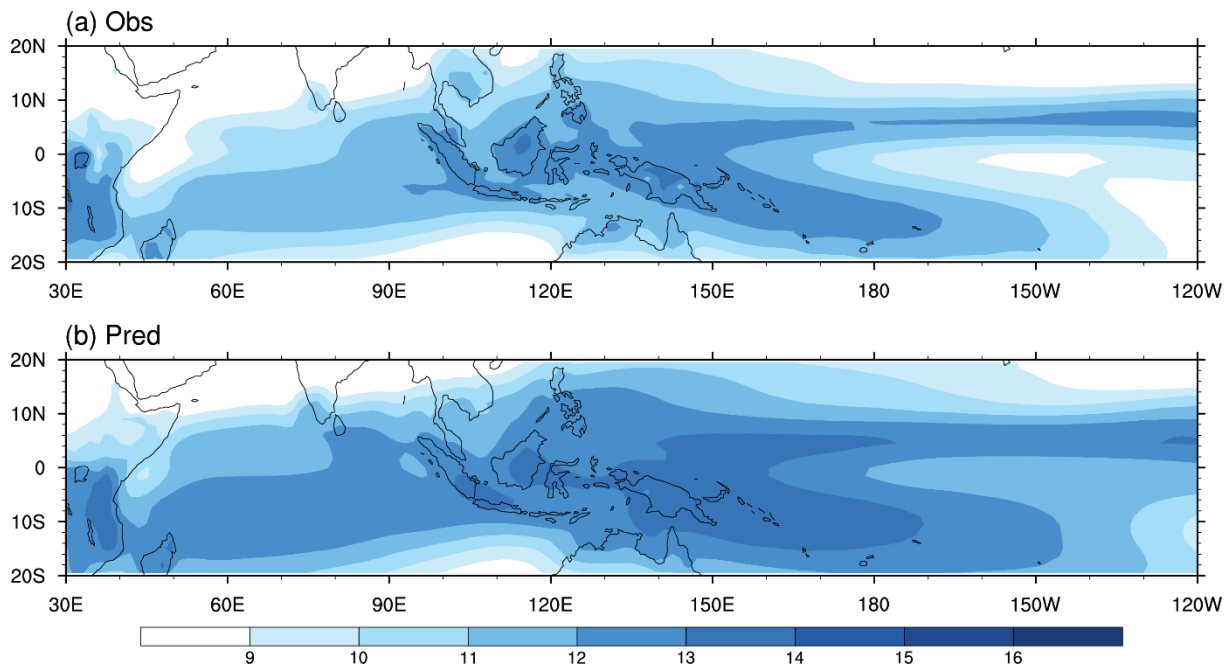
495

496

497

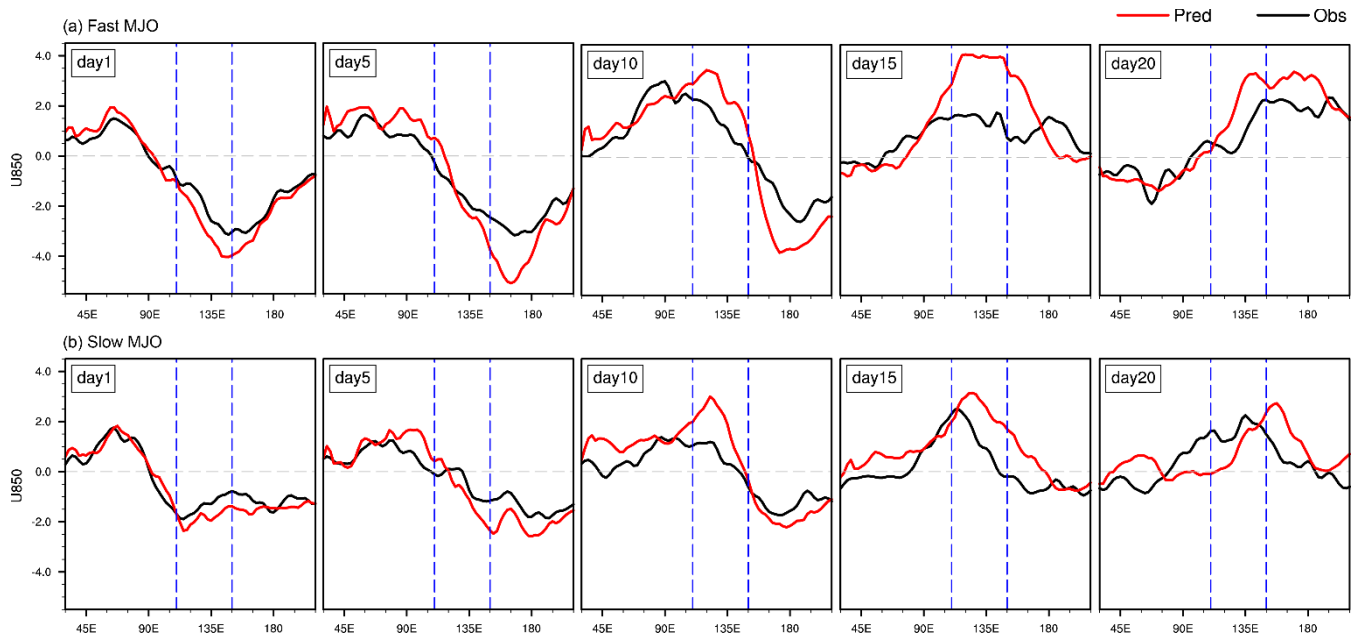
498

Figure 9. The composed longitude-vertical structure of precipitation heating (contours; $1 \times 10^{-2} \text{ J kg}^{-1} \text{ s}^{-1}$) and zonal and vertical winds anomalies (vectors; units are m/s for zonal winds and 0.01 Pa s^{-1} for vertical winds) averaged over $10^\circ \text{ S} - 10^\circ \text{ N}$ for day 1, day 5, day 10 in (a) observed fast MJO, (b) simulated fast MJO, (c) observed slow MJO and (d) simulated slow MJO.



499
500

Figure 10. The winter (November–April) mean specific humidity (g kg^{-1}) on 850hPa for (a) observation and (b) IAP-CAS model.



501

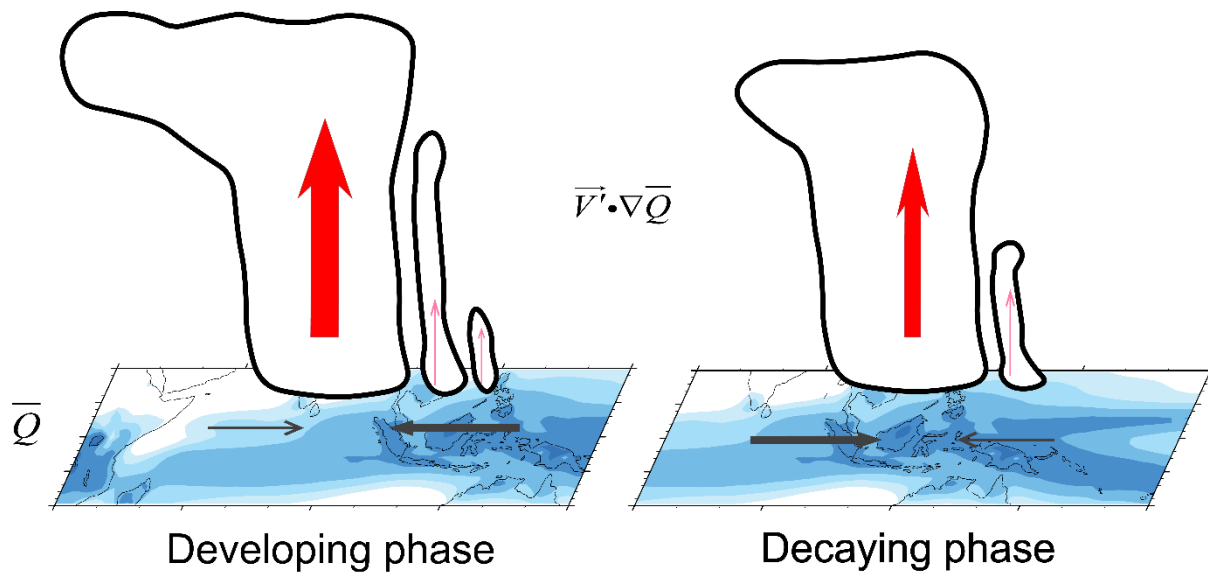
502

503

504

505

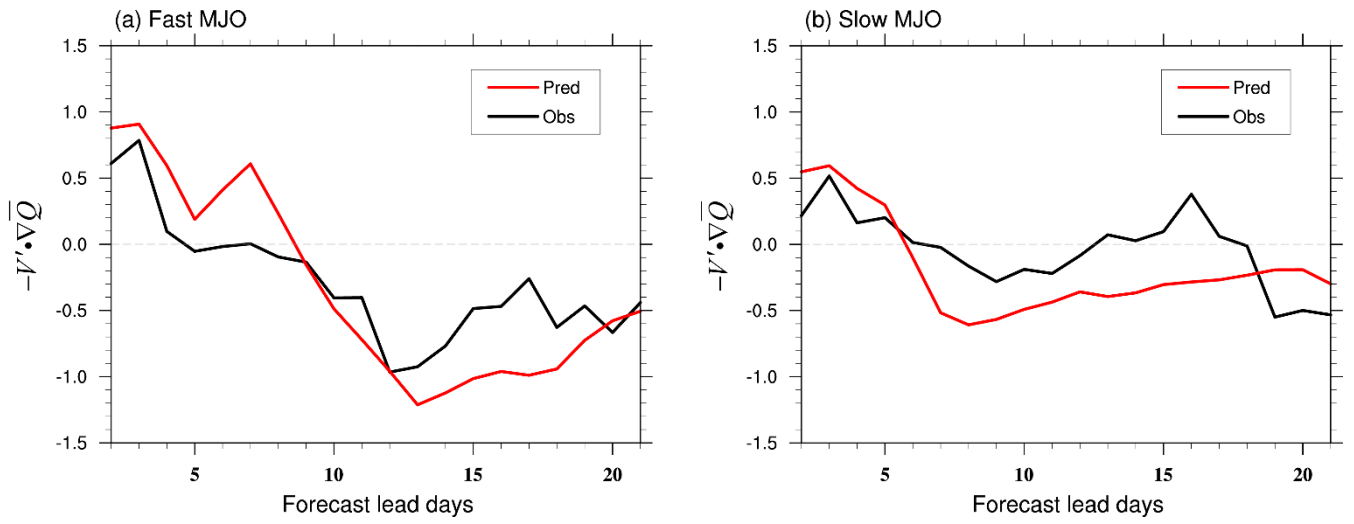
Figure 11. The composited longitudinal structure of the 850hPa zonal wind anomalies (m s^{-1}) averaged over 15°S – 15°N for day 1, day 5, day10, day15 and day 20 from observation (black solid line) and IAP-CAS model (red solid line) in fast and slow MJO events. The gray dashed line is the reference line with the values of 0. The two blue dashed lines are 110°E and 150°E respectively, which denote the extension of the MC region.



506

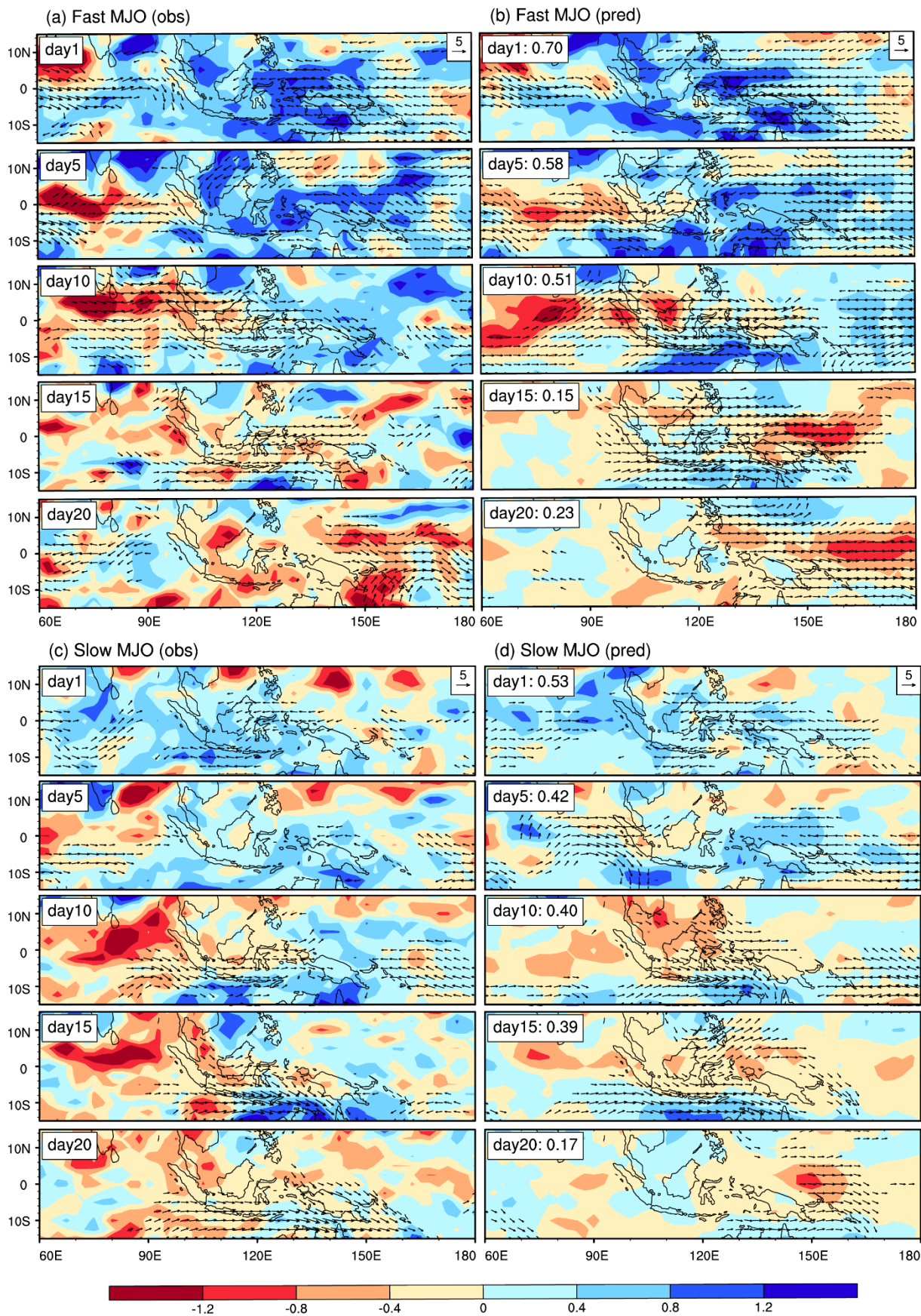
507

Figure 12. Schematic diagrams illustrating the moisture mode theory on MJO propagation in the MC region.



508

509 **Figure 13.** The composited $-V' \cdot \nabla \bar{Q}$ ($\text{g kg}^{-1} \text{s}^{-1}$) averaged over the MC region (15° S - 15° N , 110° E - 150° E) as a function of forecast
 510 lead days from observation (black solid line) and IAP-CAS model (red solid line) in (a) fast MJO and (b) slow MJO events. The gray
 511 dashed line is the reference line with the values of 0.



512
513
514
515
516

Figure 14. Evolution patterns of the composite specific humidity anomalies (g kg^{-1}) and winds (vectors; m s^{-1}) anomalies (exceeding 2 m/s) on 850hPa for day 1, day 5, day10, day15 and day 20 (a) observed fast MJO, (b) simulated fast MJO, (c) observed slow MJO and (d) simulated slow MJO. The spatial correlation coefficient between simulated and observed moisture anomalies is shown to the right of panels (b) and (c).

518 **Table A1 Hybrid coefficient of hybrid sigma-pressure coordinates at layer interfaces in CAS FGOALS-f2**

Layer	Coefficient of pressure coordinates	The coefficient of sigma coordinates	Layer	Coefficient of pressure coordinates	The coefficient of sigma coordinates
1	100.00	0.00	18	27131.33	0.23
2	400.00	0.00	19	24406.11	0.32
3	818.60	0.00	20	21326.05	0.42
4	1378.89	0.00	21	18221.18	0.51
5	2091.80	0.00	22	15275.15	0.59
6	2983.64	0.00	23	12581.68	0.67
7	4121.79	0.00	24	10181.43	0.73
8	5579.22	0.00	25	8081.90	0.79
9	7419.79	0.00	26	6270.87	0.83
10	9704.83	0.00	27	4725.35	0.87
11	12496.34	0.00	28	3417.39	0.91
12	15855.26	0.00	29	2317.75	0.93
13	19839.62	0.00	30	1398.09	0.96
14	24502.73	0.00	31	632.50	0.98
15	28177.10	0.02	32	0.00	0.99
16	29525.28	0.06	33	0.00	1.00
17	29016.34	0.14			

519 **Table A2 Initialization information of the S2S ensemble forecast system**

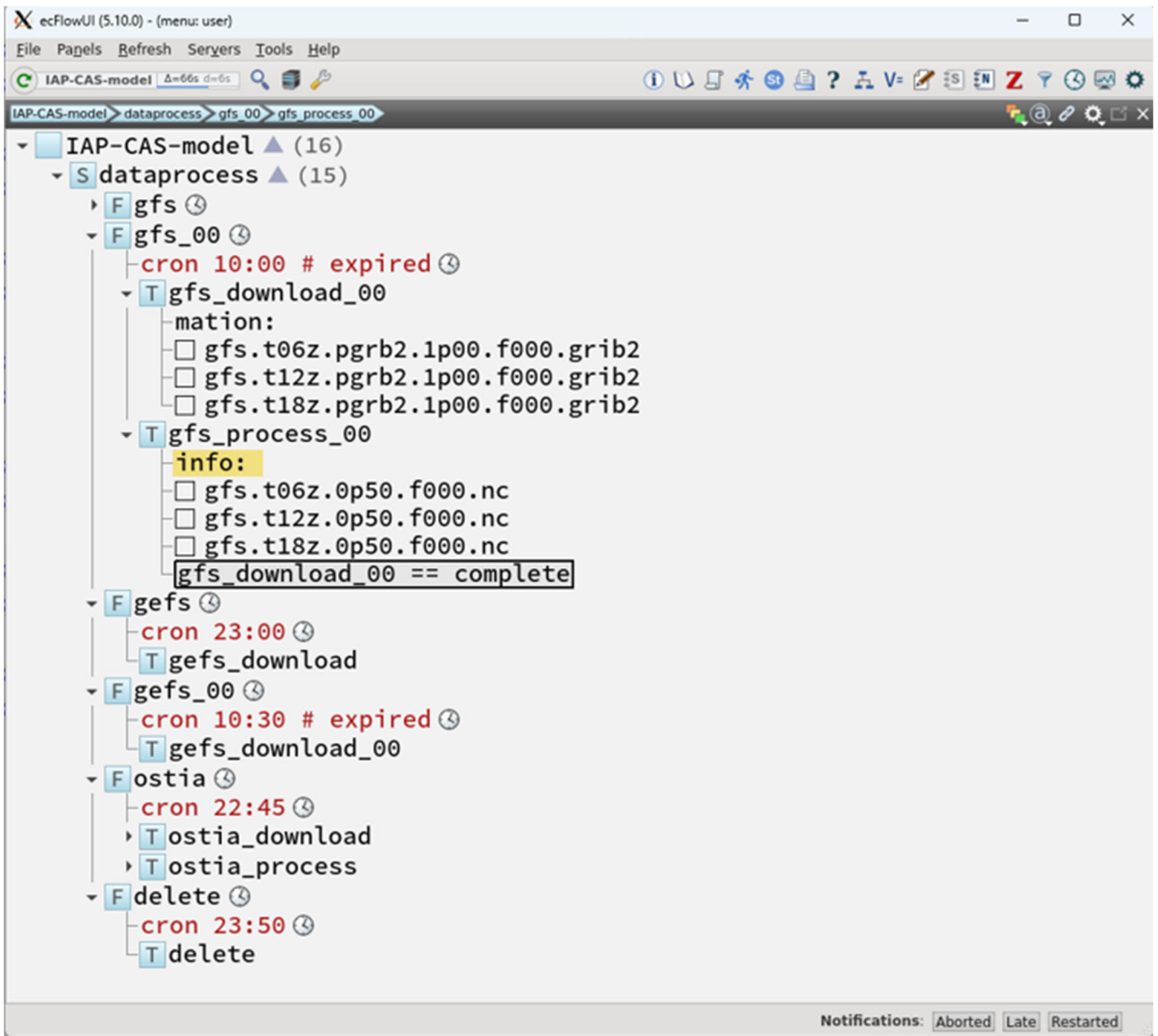
Nudging type	Data Assimilation	Variable	Data	Frequency
Reanalysis nudging	Time-Lagged Nudging (Hoffman and Kalnay, 1983; Jeuken et al., 1996)	U, V, T, P _s , z _s ^a SST	FNL (http://rda.ucar.edu/datasets/ds083.2 , ds083.2 DOI: 10.5065/D6M043C6) NOAA OISST (Reynolds et al., 2007)	6h
Forecast nudging		U, V, T, P _s , z _s	GFS weather forecast	6h

520 ^a Table notes: U represents zonal wind, V represents meridional wind, T represents temperature, P_s represents surface pressure,
521 z_s represents surface geopotential height, and SST represents sea surface temperature.

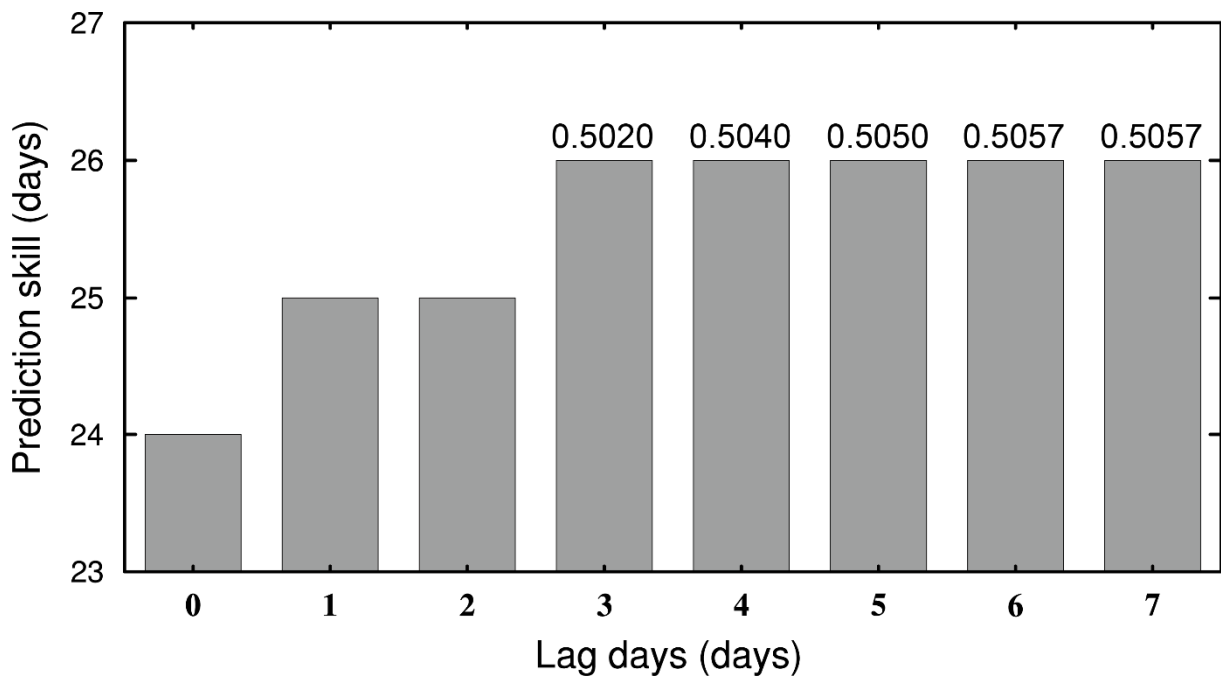
Experiment	Ensemble members	Time range	Frequency	Forecast time	Variable	Resolution	Interpolation method
Hindcast	4	1999-2018	Daily	65 days	25 variables	Horizontal:1.5°	One-order
Real-time forecast	16	2019			(A detailed list of variables is shown in TableA4)	×1.5° Vertical:7 levels (1000, 925, 850, 700, 500, 300, and 200hPa)	conservation

Statistical process	Level(s)	Short name	Standard name	Unit	
Instantaneous value/24h	The variables are located on 10 pressure layers (1000, 925, 850, 700, 500, 300, 200, 100, 50, 10 hPa)	gh	Geopotential height	gpm	
		t	Temperature	K	
		u	U-velocity	m s ⁻¹	
		v	V-velocity	m s ⁻¹	
		w	Vertical velocity	pa s ⁻¹	
	The variable is located on 7 pressure layers (1000, 925, 850, 700, 500, 300, 200 hPa)	q	Specific humidity	kg kg ⁻¹	
		2-dimensional variables	w	Vertical velocity	pa s ⁻¹
			sp	Surface pressure	Pa
			lsm	Land sea mask	Proportion of land
			orog	Orography	gpm
Daily average value		tcc	Total cloud cover	%	
		skt	Skin temperature	K	
		2t	Surface air temperature	K	
		2d	Surface air dewpoint temperature	2d	
		wtmp	Sea surface temperature	K	
		ci	Sea ice cover	proportion	

24-hour accumulated value	sf	Snow fall water equivalent	kg m ⁻²
	ttr	Time-integrated top net thermal radiation	W m ⁻² s
	ssr	Time-integrated surface net solar radiation	W m ⁻² s
	str	Time-integrated surface net thermal radiation	W m ⁻² s
	ssrd	Time-integrated surface solar radiation downwards	W m ⁻² s
	strd	Time-integrated surface thermal radiation downwards	W m ⁻² s
Instantaneous value/6h	mx2t6	Surface air maximum temperature	K
	mn2t6	Surface air minimum temperature	K
	10u	10 metre u-velocity	m s ⁻¹
	10v	10 metre v-velocity	m s ⁻¹
6-hour accumulated value	tp	Total precipitation	kg m ⁻²



525
 526 **Figure A1.** The structure of ecFlow (ECMWF Workflow). EcFlow, developed and maintained by the ECMWF, is a client/server
 527 workflow package designed to facilitate the execution of a substantial number of programs within a controlled environment. It is
 528 used in the IAP-CAS model to accomplish the download and preprocessing of the forcing data.



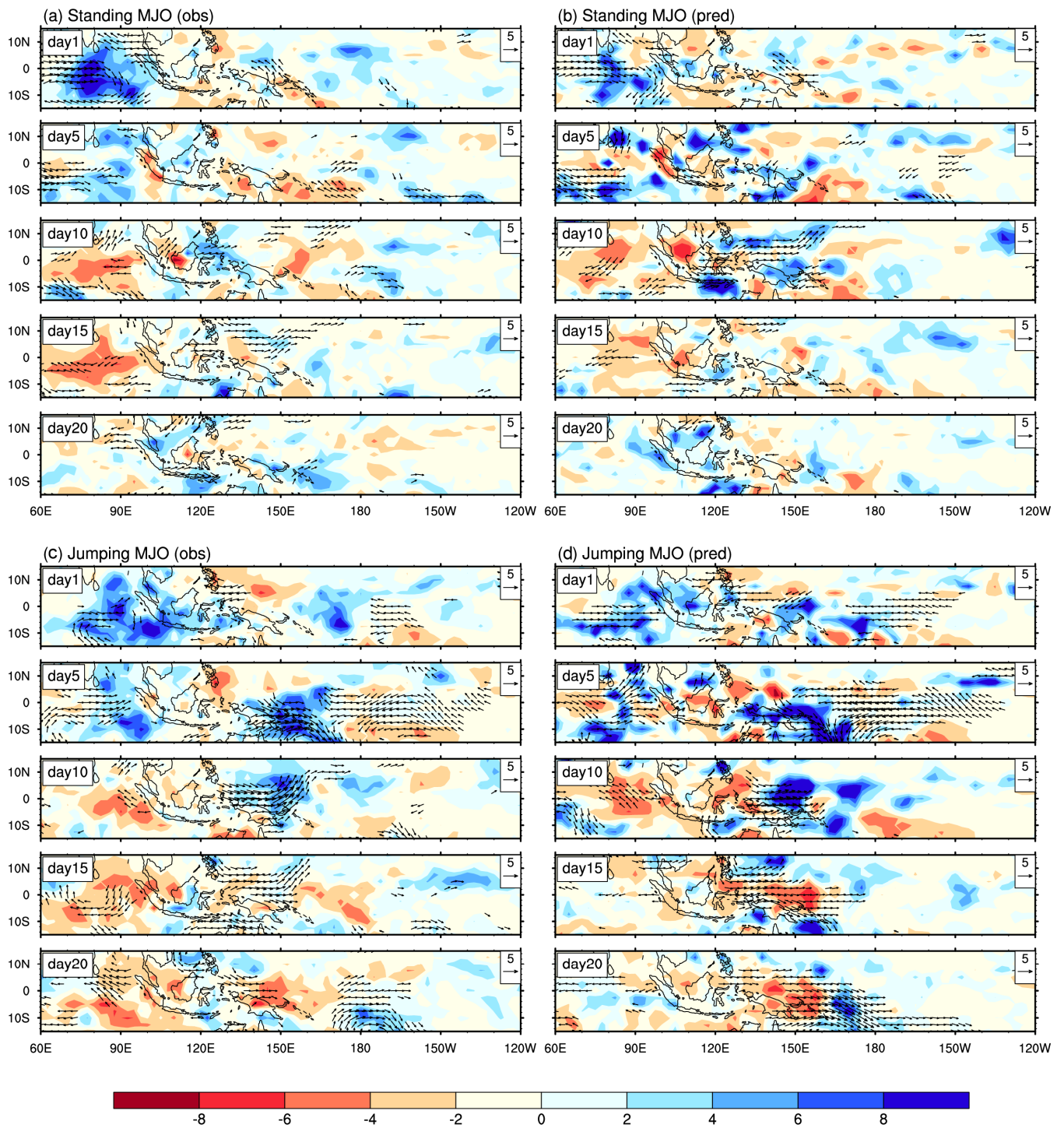
529

530

Figure A2. MJO forecast skill of the ensemble mean of time-lagged members as a function of lag days. The values on the bars represent the ACC on day 26.

531

532



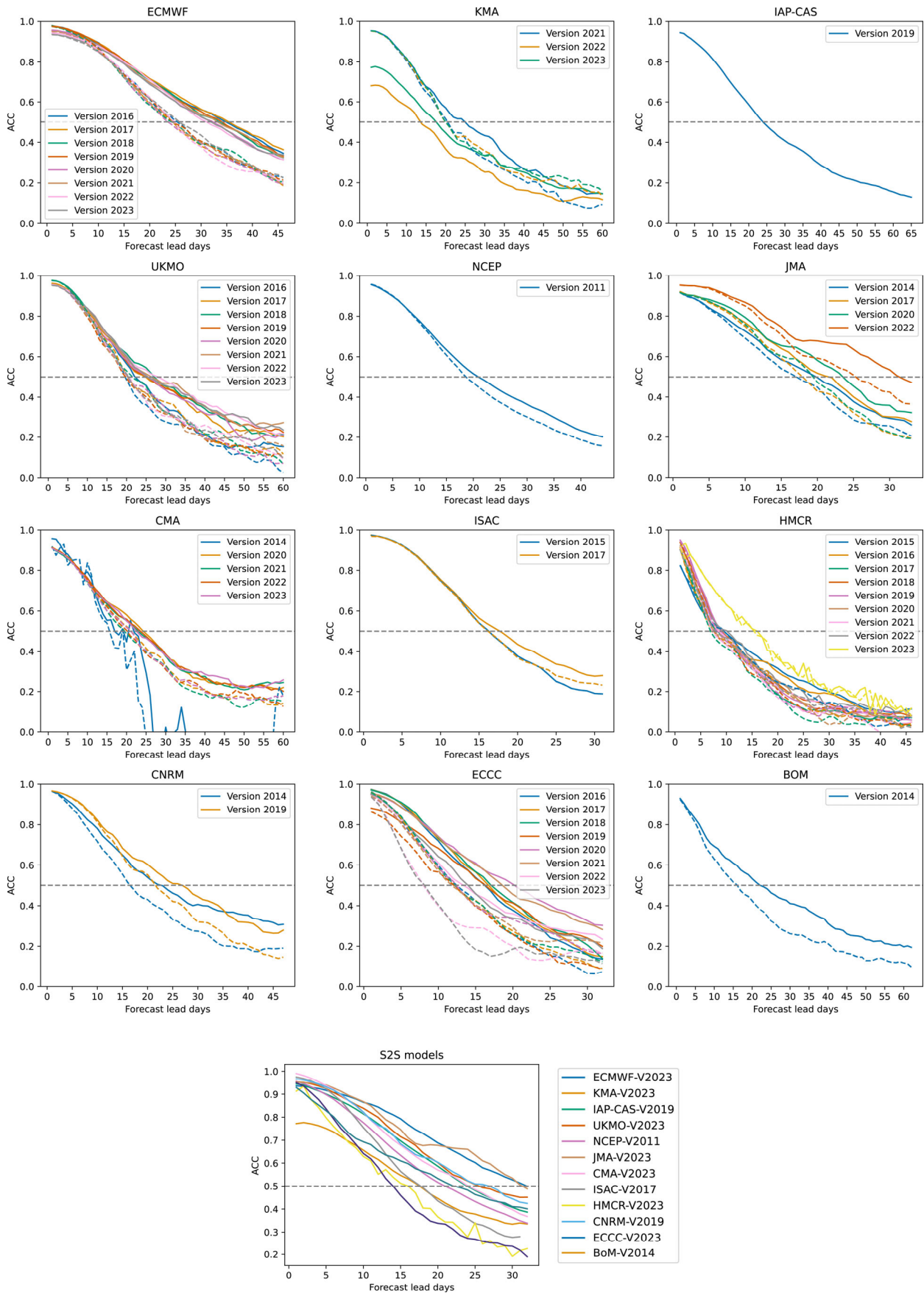
533

534

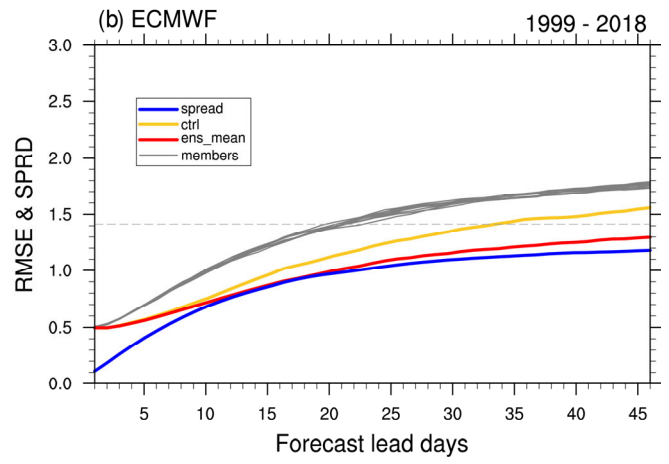
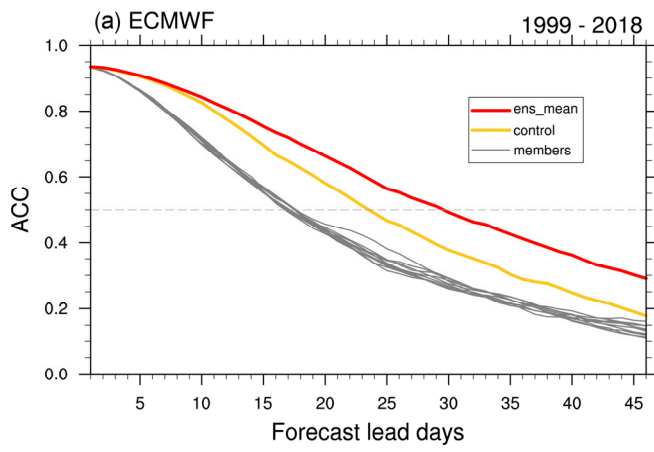
535

536

Figure A3. Evolution patterns of the composite precipitation (shading; mm day⁻¹) and 850-hPa winds (vectors; m s⁻¹) anomalies (exceeding 2 m/s) for day 1, day 5, day10, day15 and day 20 in (a) observed standing MJO, (b) simulated standing MJO, (c) observed Jumping MJO and (d) simulated Jumping MJO.



537
 538 **Figure A4. The MJO forecast skill of 12 S2S models, providing comparisons between various model versions over the years, and the**
 539 **latest versions of 12 models. The evaluation covers the period from 2001 to 2010, except for CMA, which spans from 2008 to 2013.**
 540 **The solid lines represent the skill of ensemble mean forecasts, while the dashed lines represent the skill of deterministic forecasts.**



541

542

Figure A5. The ACC (a) and the RMSE (b) of ECMWF (2019 version) from individual members (gray solid line), ensemble ctrl (yellow solid line), and 10-member ensemble mean (red solid line) as a function of forecast lead days. The blue solid line denotes the ensemble spread. The dashed line in (a) has a value of 0.5, and it represents 1.414 in (b).

543

544

545

546 **Code availability**

547 The code of the IAP-CAS model is archived on Zenodo (<https://doi.org/10.5281/zenodo.10791355>). The code used to
548 reproduce the figures in this work can be obtained from <https://doi.org/10.5281/zenodo.10817813>.

549 **Data availability**

550 The boundary conditions and input data are available at <https://doi.org/10.5281/zenodo.10820243>. The data for initial
551 ization in the IAP-CAS S2S system is available at <http://rda.ucar.edu/datasets/ds083.2>, ds083.2[DOI: 10.5065/D6M043-
552 C6 (FNL), <https://www.ncei.noaa.gov/products/optimum-interpolation-sst> (NOAA OISST) and [https://www.ncei.noaa.gov/
553 v/products/weather-climate-models/global-forecast](https://www.ncei.noaa.gov/products/weather-climate-models/global-forecast) (GFS weather forecast). The hindcast dataset of the IAP-CAS S2S
554 system used in the article is publicly available on the three S2S Data Portals (ECMWF: [https://apps.ecmwf.int/data-
555 sets/](https://apps.ecmwf.int/datasets/); CMA: <http://s2s.cma.cn/index>; IRI: <https://iridl.ldeo.columbia.edu/SOURCES/ECMWF/S2S/>). All the validation
556 data are available to download from the cited references or data links shown in Section 3.1.

557 **Author contribution**

558 Q.B. led the IAP-CAS model development. All other co-authors contributed to it. B.H. and X.F.W. designed the experiments
559 and carried them out. Y.K.L. utilized the dataset to assess the performance of the IAP-CAS S2S system and wrote the final
560 document with contributions from all other authors. Q.B. reviewed and edited the manuscript. G.X.W., Y.M.L., and J.Y.
561 supervised and supported this research and gave important opinions.

562 **Competing interests**

563 The authors declare no conflict of interest.

564 **Acknowledgments**

565 This work was supported by funding from the National Natural Science Foundation of China (Grant 42175161, 42261144671),
566 the Alliance of International Science Organizations (Grant ANSO-CR-KP-2020-01), and the National Key Scientific and
567 Technological Infrastructure project “Earth System Numerical Simulation Facility”.

568 **References**

569 Adames, Á. F. and Kim, D.: The MJO as a Dispersive, Convectively Coupled Moisture Wave: Theory and Observations,
570 *Journal of the Atmospheric Sciences*, 73, 913–941, <https://doi.org/10.1175/JAS-D-15-0170.1>, 2016.

571 Adames, Á. F. and Wallace, J. M.: Three-Dimensional Structure and Evolution of the MJO and Its Relation to the Mean Flow,
572 *Journal of the Atmospheric Sciences*, 71, 2007–2026, <https://doi.org/10.1175/JAS-D-13-0254.1>, 2014.

573 Adames, Á. F. and Wallace, J. M.: Three-Dimensional Structure and Evolution of the Moisture Field in the MJO, *Journal of*
574 *the Atmospheric Sciences*, 72, 3733–3754, <https://doi.org/10.1175/JAS-D-15-0003.1>, 2015.

575 Adler, R. F., Huffman, G. J., Chang, A., Ferraro, R., Xie, P.-P., Janowiak, J., Rudolf, B., Schneider, U., Curtis, S., Bolvin, D.,
576 Gruber, A., Susskind, J., Arkin, P., and Nelkin, E.: The Version-2 Global Precipitation Climatology Project (GPCP) Monthly
577 Precipitation Analysis (1979–Present), *Journal of Hydrometeorology*, 4, 1147–1167, [https://doi.org/10.1175/1525-7541\(2003\)004<1147:TVGPCP>2.0.CO;2](https://doi.org/10.1175/1525-7541(2003)004<1147:TVGPCP>2.0.CO;2), 2003.

579 Ahn, M., Kim, D., Kang, D., Lee, J., Sperber, K. R., Gleckler, P. J., Jiang, X., Ham, Y., and Kim, H.: MJO Propagation Across
580 the Maritime Continent: Are CMIP6 Models Better Than CMIP5 Models?, *Geophysical Research Letters*, 47,
581 <https://doi.org/10.1029/2020GL087250>, 2020.

582 Ahn, M. S., Kim, D., Kang, D., Lee, J., Sperber, K. R., and Gleckler, P. J.: MJO Simulation in CMIP6 Models: How much
583 improvement has been made from CMIP5 to CMIP6?, 2019, A41G-04, 2019.

584 Bao, Q.: Outlook for El Niño and the Indian Ocean Dipole in autumn-winter 2018–2019, *CSB*, 73–78,
585 <https://doi.org/10.1360/N972018-00913>, 2019.

586 Bao, Q. and Li, J.: Progress in climate modeling of precipitation over the Tibetan Plateau, *National Science Review*, 7, 486–
587 487, <https://doi.org/10.1093/nsr/nwaa006>, 2020.

588 Bao, Q., Liu, Y., Wu, G., He, B., Li, J., Wang, L., Wu, X., Chen, K., Wang, X., Yang, J., and Zhang, X.: CAS FGOALS-f3-
589 H and CAS FGOALS-f3-L outputs for the high-resolution model intercomparison project simulation of CMIP6, *Atmospheric*
590 *and Oceanic Science Letters*, 13, 576–581, <https://doi.org/10.1080/16742834.2020.1814675>, 2020.

591 Benedict, J. J. and Randall, D. A.: Observed Characteristics of the MJO Relative to Maximum Rainfall, *Journal of the*
592 *Atmospheric Sciences*, 64, 2332–2354, <https://doi.org/10.1175/JAS3968.1>, 2007.

593 Bessafi, M. and Wheeler, M. C.: Modulation of south Indian ocean tropical cyclones by the Madden-Julian oscillation and
594 convectively coupled equatorial waves, *Mon. Weather Rev.*, 134, 638–656, <https://doi.org/10.1175/MWR3087.1>, 2006.

595 Cassou, C.: Intraseasonal interaction between the Madden–Julian Oscillation and the North Atlantic Oscillation, *Nature*, 455,
596 523–527, <https://doi.org/10.1038/nature07286>, 2008.

597 Chen, G., Ling, J., Zhang, R., Xiao, Z., and Li, C.: The MJO From CMIP5 to CMIP6: Perspectives From Tracking MJO
598 Precipitation, *Geophysical Research Letters*, 49, <https://doi.org/10.1029/2021GL095241>, 2022.

599 Craig, A. P., Vertenstein, M., and Jacob, R.: A new flexible coupler for earth system modeling developed for CCSM4 and
600 CESM1, *The International Journal of High Performance Computing Applications*, 26, 31–42,
601 <https://doi.org/10.1177/1094342011428141>, 2012.

602 Crueger, T., Stevens, B., and Brokopf, R.: The Madden-Julian Oscillation in ECHAM6 and the Introduction of an Objective
603 MJO Metric, *J. Clim.*, 26, 3241–3257, <https://doi.org/10.1175/JCLI-D-12-00413.1>, 2013.

604 DeMott, C. A., Wolding, B. O., Maloney, E. D., and Randall, D. A.: Atmospheric Mechanisms for MJO Decay Over the
605 Maritime Continent, *Journal of Geophysical Research: Atmospheres*, 123, 5188–5204, <https://doi.org/10.1029/2017JD026979>,
606 2018.

607 ERA, C.: Fifth generation of ECMWF atmospheric reanalyses of the global climate, Copernicus Climate Change Service
608 Climate Data Store (CDS), 2017.

609 Ferreira, R. N., Schubert, W. H., and Hack, J. J.: Dynamical aspects of twin tropical cyclones associated with the Madden-
610 Julian oscillation, *J. Atmos. Sci.*, 53, 929–945, [https://doi.org/10.1175/1520-0469\(1996\)053<0929:DAOTTC>2.0.CO;2](https://doi.org/10.1175/1520-0469(1996)053<0929:DAOTTC>2.0.CO;2), 1996.

611 Gonzalez, A. O. and Jiang, X.: Winter mean lower tropospheric moisture over the Maritime Continent as a climate model
612 diagnostic metric for the propagation of the Madden-Julian oscillation, *Geophysical Research Letters*, 44, 2588–2596,
613 <https://doi.org/10.1002/2016GL072430>, 2017.

614 Goswami, B. N.: South asian monsoon, Springer, 2012.

615 Gottschalck, J., Wheeler, M., Weickmann, K., Vitart, F., Savage, N., Lin, H., Hendon, H., Waliser, D., Sperber, K., Nakagawa,
616 M., Prestrelo, C., Flatau, M., and Higgins, W.: A Framework for Assessing Operational Madden–Julian Oscillation Forecasts:
617 A CLIVAR MJO Working Group Project, *Bull. Amer. Meteor. Soc.*, 91, 1247–1258,
618 <https://doi.org/10.1175/2010BAMS2816.1>, 2010.

619 Hall, J. D., Matthews, A. J., and Karoly, D. J.: The modulation of tropical cyclone activity in the Australian region by the
620 Madden-Julian oscillation, *Mon. Weather Rev.*, 129, 2970–2982, [https://doi.org/10.1175/1520-0493\(2001\)129<2970:TMOTCA>2.0.CO;2](https://doi.org/10.1175/1520-0493(2001)129<2970:TMOTCA>2.0.CO;2), 2001.

622 Hannah, W. M., Maloney, E. D., and Pritchard, M. S.: Consequences of systematic model drift in DYNAMO MJO hindcasts
623 with SP-CAM and CAM5, *Journal of Advances in Modeling Earth Systems*, 7, 1051–1074,
624 <https://doi.org/10.1002/2014MS000423>, 2015.

625 Harris, L., Zhou, L., Lin, S.-J., Chen, J.-H., Chen, X., Gao, K., Morin, M., Rees, S., Sun, Y., Tong, M., Xiang, B., Bender, M.,
626 Benson, R., Cheng, K.-Y., Clark, S., Elbert, O. D., Hazelton, A., Huff, J. J., Kaltenbaugh, A., Liang, Z., Marchok, T., Shin, H.
627 H., and Stern, W.: GFDL SHIELD: A Unified System for Weather-to-Seasonal Prediction, *Journal of Advances in Modeling*
628 *Earth Systems*, 12, e2020MS002223, <https://doi.org/10.1029/2020MS002223>, 2020.

629 Harris, L. M. and Lin, S.-J.: A Two-Way Nested Global-Regional Dynamical Core on the Cubed-Sphere Grid, *Monthly*
630 *Weather Review*, 141, 283–306, <https://doi.org/10.1175/MWR-D-11-00201.1>, 2013.

631 Hendon, H. H. and Salby, M. L.: The Life Cycle of the Madden–Julian Oscillation, *Journal of the Atmospheric Sciences*, 51,
632 2225–2237, [https://doi.org/10.1175/1520-0469\(1994\)051<2225:TLCOTM>2.0.CO;2](https://doi.org/10.1175/1520-0469(1994)051<2225:TLCOTM>2.0.CO;2), 1994.

633 Ho, C.-H., Kim, J.-H., Jeong, J.-H., Kim, H.-S., and Chen, D.: Variation of tropical cyclone activity in the South Indian Ocean:
634 El Niño–Southern Oscillation and Madden-Julian Oscillation effects, *J. Geophys. Res.*, 111, D22101,
635 <https://doi.org/10.1029/2006JD007289>, 2006.

636 Hoffman, R. N. and Kalnay, E.: Lagged average forecasting, an alternative to Monte Carlo forecasting, *Tellus A: Dynamic*
637 *Meteorology and Oceanography*, 35, 100–118, <https://doi.org/10.3402/tellusa.v35i2.11425>, 1983.

638 Hsu, H. H. and Lee, M. Y.: Topographic effects on the eastward propagation and initiation of the Madden-Julian oscillation,
639 *J. Clim.*, 18, 795–809, <https://doi.org/10.1175/JCLI-3292.1>, 2005.

640 Hsu, H.-H.: Intraseasonal variability of the atmosphere–ocean–climate system: East Asian monsoon, in: *Intraseasonal*
641 *Variability in the Atmosphere-Ocean Climate System*, edited by: Lau, W. K.-M. and Waliser, D. E., Springer Berlin Heidelberg,
642 Berlin, Heidelberg, 73–110, https://doi.org/10.1007/978-3-642-13914-7_3, 2012.

643 Hsu, P. and Li, T.: Role of the Boundary Layer Moisture Asymmetry in Causing the Eastward Propagation of the Madden–
644 Julian Oscillation, *Journal of Climate*, 25, 4914–4931, <https://doi.org/10.1175/JCLI-D-11-00310.1>, 2012.

645 Hung, M.-P., Lin, J.-L., Wang, W., Kim, D., Shinoda, T., and Weaver, S. J.: MJO and Convectively Coupled Equatorial Waves
646 Simulated by CMIP5 Climate Models, *Journal of Climate*, 26, 6185–6214, <https://doi.org/10.1175/JCLI-D-12-00541.1>, 2013.

647 Hunke, E. C., Lipscomb, W. H., Turner, A. K., Jeffery, N., and Elliott, S.: Cice: the los alamos sea ice model documentation
648 and software user’s manual version 4.1 la-cc-06-012, T-3 Fluid Dynamics Group, Los Alamos National Laboratory, 675, 500,
649 2010.

650 Inness, P. M. and Slingo, J. M.: The interaction of the Madden-Julian Oscillation with the Maritime Continent in a GCM, *Q.*
651 *J. R. Meteorol. Soc.*, 132, 1645–1667, <https://doi.org/10.1256/qj.05.102>, 2006.

652 Jeuken, A. B. M., Siegmund, P. C., Heijboer, L. C., Feichter, J., and Bengtsson, L.: On the potential of assimilating
653 meteorological analyses in a global climate model for the purpose of model validation, *Journal of Geophysical Research:*
654 *Atmospheres*, 101, 16939–16950, <https://doi.org/10.1029/96JD01218>, 1996.

655 Jiang, X.: Key processes for the eastward propagation of the Madden-Julian Oscillation based on multimodel simulations: Key
656 Model Processes for MJO Propagation, *J. Geophys. Res. Atmos.*, 122, 755–770, <https://doi.org/10.1002/2016JD025955>, 2017.

657 Jiang, X., Adames, Á. F., Zhao, M., Waliser, D., and Maloney, E.: A Unified Moisture Mode Framework for Seasonality of
658 the Madden–Julian Oscillation, *Journal of Climate*, 31, 4215–4224, <https://doi.org/10.1175/JCLI-D-17-0671.1>, 2018.

659 Kanamitsu, M., Ebisuzaki, W., Woollen, J., Yang, S.-K., Hnilo, J. J., Fiorino, M., and Potter, G. L.: NCEP–DOE AMIP-II
660 Reanalysis (R-2), *Bulletin of the American Meteorological Society*, 83, 1631–1644, [https://doi.org/10.1175/BAMS-83-11-](https://doi.org/10.1175/BAMS-83-11-1631)
661 1631, 2002.

662 Kemball-Cook, S. R. and Weare, B. C.: The Onset of Convection in the Madden–Julian Oscillation, *J. Climate*, 14, 780–793,
663 [https://doi.org/10.1175/1520-0442\(2001\)014<0780:TOOCIT>2.0.CO;2](https://doi.org/10.1175/1520-0442(2001)014<0780:TOOCIT>2.0.CO;2), 2001.

664 Kerbyson, D. J. and Jones, P. W.: A Performance Model of the Parallel Ocean Program, *The International Journal of High*
665 *Performance Computing Applications*, 19, 261–276, <https://doi.org/10.1177/1094342005056114>, 2005.

666 Kim, D., Kug, J.-S., and Sobel, A. H.: Propagating versus Nonpropagating Madden–Julian Oscillation Events, *Journal of*
667 *Climate*, 27, 111–125, <https://doi.org/10.1175/JCLI-D-13-00084.1>, 2014a.

668 Kim, H.: MJO Propagation Processes and Mean Biases in the SubX and S2S Reforecasts, *J. Geophys. Res. Atmos.*, 124, 9314–
669 9331, <https://doi.org/10.1029/2019JD031139>, 2019.

670 Kim, H., Vitart, F., and Waliser, D. E.: Prediction of the Madden–Julian Oscillation: A Review, *J Climate*, 31, 9425–9443,
671 <https://doi.org/10.1175/JCLI-D-18-0210.1>, 2018.

672 Kim, H.-M.: The impact of the mean moisture bias on the key physics of MJO propagation in the ECMWF reforecast, *Journal*
673 *of Geophysical Research: Atmospheres*, 122, 7772–7784, <https://doi.org/10.1002/2017JD027005>, 2017.

674 Kim, H.-M., Webster, P. J., Toma, V. E., and Kim, D.: Predictability and Prediction Skill of the MJO in Two Operational
675 Forecasting Systems, *J Climate*, 27, 5364–5378, <https://doi.org/10.1175/JCLI-D-13-00480.1>, 2014b.

676 Lau, K.-M. and Chan, P. H.: Aspects of the 40–50 Day Oscillation during the Northern Summer as Inferred from Outgoing
677 Longwave Radiation, *Monthly Weather Review*, 114, 1354–1367, [https://doi.org/10.1175/1520-0493\(1986\)114<1354:AOTDOD>2.0.CO;2](https://doi.org/10.1175/1520-0493(1986)114<1354:AOTDOD>2.0.CO;2), 1986.

678 Lau, W. K., Waliser, D. E., and Lau, W. K.: El Nino southern oscillation connection, Springer, 2005.

679 Lawrence, D. M., Oleson, K. W., Flanner, M. G., Thornton, P. E., Swenson, S. C., Lawrence, P. J., Zeng, X., Yang, Z.-L.,
680 Levis, S., Sakaguchi, K., Bonan, G. B., and Slater, A. G.: Parameterization improvements and functional and structural
681 advances in Version 4 of the Community Land Model: PARAMETERIZATION IMPROVEMENTS AND FUNCTIONAL
682 AND STRUCTURAL ADVANCES, *J. Adv. Model. Earth Syst.*, 3, n/a-n/a, <https://doi.org/10.1029/2011MS00045>, 2011.

683 Leutbecher, M. and Palmer, T. N.: Ensemble forecasting, *Journal of Computational Physics*, 227, 3515–3539,
684 <https://doi.org/10.1016/j.jcp.2007.02.014>, 2008.

685 Li, J., Bao, Q., Liu, Y., Wu, G., Wang, L., He, B., Wang, X., and Li, J.: Evaluation of FAMIL2 in Simulating the Climatology
686 and Seasonal-to-Interannual Variability of Tropical Cyclone Characteristics, *J. Adv. Model. Earth Syst.*, 11, 1117–1136,
687 <https://doi.org/10.1029/2018MS001506>, 2019.

688 Liebmann, B. and Smith, C. A.: Description of a Complete (Interpolated) Outgoing Longwave Radiation Dataset, *Bulletin of*
689 *the American Meteorological Society*, 77, 1275–1277, 1996.

690 Liebmann, B., Hendon, H., and Glick, J.: The Relationship Between Tropical Cyclones of the Western Pacific and Indian
691 Oceans and the Madden-Julian Oscillation, *J. Meteorol. Soc. Jpn.*, 72, 401–412, https://doi.org/10.2151/jmsj1965.72.3_401,
692 1994.

693 Lim, Y., Son, S.-W., and Kim, D.: MJO Prediction Skill of the Subseasonal-to-Seasonal Prediction Models, *Journal of Climate*,
694 31, 4075–4094, <https://doi.org/10.1175/JCLI-D-17-0545.1>, 2018.

695

696 Lin, H., Brunet, G., and Derome, J.: Forecast Skill of the Madden–Julian Oscillation in Two Canadian Atmospheric Models,
697 Monthly Weather Review, 136, 4130–4149, <https://doi.org/10.1175/2008MWR2459.1>, 2008.

698 Lin, S.-J.: A “Vertically Lagrangian” Finite-Volume Dynamical Core for Global Models, Monthly Weather Review, 132,
699 2293–2307, [https://doi.org/10.1175/1520-0493\(2004\)132<2293:AVLFDC>2.0.CO;2](https://doi.org/10.1175/1520-0493(2004)132<2293:AVLFDC>2.0.CO;2), 2004.

700 Lin, Y., Farley, R., and Orville, H.: Bulk Parameterization of the Snow Field in a Cloud Model, JOURNAL OF CLIMATE
701 AND APPLIED METEOROLOGY, 22, 1065–1092, [https://doi.org/10.1175/1520-0450\(1983\)022<1065:BPOTSF>2.0.CO;2](https://doi.org/10.1175/1520-0450(1983)022<1065:BPOTSF>2.0.CO;2),
702 1983.

703 Liu, F., Wang, B., Ouyang, Y., Wang, H., Qiao, S., Chen, G., and Dong, W.: Intraseasonal variability of global land monsoon
704 precipitation and its recent trend, npj Clim Atmos Sci, 5, 30, <https://doi.org/10.1038/s41612-022-00253-7>, 2022.

705 Liu, Y. Q.: Prediction of monthly-seasonal precipitation using coupled SVD patterns between soil moisture and subsequent
706 precipitation, Geophys. Res. Lett., 30, 1827, <https://doi.org/10.1029/2003GL017709>, 2003.

707 Lorenz, E. N.: Predictability: A problem partly solved, in Proceedings of Seminar on Predictability, 4–8 September 1995, 1996.

708 Madden, R. A. and Julian, P. R.: Detection of a 40–50 Day Oscillation in the Zonal Wind in the Tropical Pacific, Journal of
709 the Atmospheric Sciences, 28, 702–708, [https://doi.org/10.1175/1520-0469\(1971\)028<0702:DOADOI>2.0.CO;2](https://doi.org/10.1175/1520-0469(1971)028<0702:DOADOI>2.0.CO;2), 1971.

710 Maloney, E. D.: An Intraseasonal Oscillation Composite Life Cycle in the NCAR CCM3.6 with Modified Convection, J.
711 Climate, 15, 964–982, [https://doi.org/10.1175/1520-0442\(2002\)015<0964:AIOCLC>2.0.CO;2](https://doi.org/10.1175/1520-0442(2002)015<0964:AIOCLC>2.0.CO;2), 2002.

712 Maloney, E. D. and Hartmann, D. L.: Modulation of eastern North Pacific hurricanes by the Madden-Julian oscillation, J.
713 Clim., 13, 1451–1460, [https://doi.org/10.1175/1520-0442\(2000\)013<1451:MOENPH>2.0.CO;2](https://doi.org/10.1175/1520-0442(2000)013<1451:MOENPH>2.0.CO;2), 2000.

714 Mu, M., Duan, W. S., and Wang, B.: Conditional nonlinear optimal perturbation and its applications, Nonlinear Processes in
715 Geophysics, 10, 493–501, <https://doi.org/10.5194/npg-10-493-2003>, 2003.

716 Nasuno, T., Li, T., and Kikuchi, K.: Moistening Processes before the Convective Initiation of Madden–Julian Oscillation
717 Events during the CINDY2011/DYNAMO Period, Monthly Weather Review, 143, 622–643, [https://doi.org/10.1175/MWR-](https://doi.org/10.1175/MWR-D-14-00132.1)
718 [D-14-00132.1](https://doi.org/10.1175/MWR-D-14-00132.1), 2015.

719 Neena, J. M., Lee, J. Y., Waliser, D., Wang, B., and Jiang, X.: Predictability of the Madden–Julian Oscillation in the
720 Intraseasonal Variability Hindcast Experiment (ISVHE)*, J Climate, 27, 4531–4543, [https://doi.org/10.1175/JCLI-D-13-](https://doi.org/10.1175/JCLI-D-13-00624.1)
721 [00624.1](https://doi.org/10.1175/JCLI-D-13-00624.1), 2014.

722 Nerger, L., Tang, Q., and Mu, L.: Efficient ensemble data assimilation for coupled models with the Parallel Data Assimilation
723 Framework: example of AWI-CM (AWI-CM-PDAF 1.0), Geosci. Model Dev., 13, 4305–4321, [https://doi.org/10.5194/gmd-](https://doi.org/10.5194/gmd-13-4305-2020)
724 [13-4305-2020](https://doi.org/10.5194/gmd-13-4305-2020), 2020.

725 Oleson, W., Lawrence, M., Bonan, B., Flanner, G., Kluzek, E., Lawrence, J., Levis, S., Swenson, C., Thornton, E., Dai, A.,
726 Decker, M., Dickinson, R., Feddema, J., Heald, L., Hoffman, F., Lamarque, J.-F., Mahowald, N., Niu, G.-Y., Qian, T.,

727 Randerson, J., Running, S., Sakaguchi, K., Slater, A., Stockli, R., Wang, A., Yang, Z.-L., Zeng, X., and Zeng, X.: Technical
728 Description of version 4.0 of the Community Land Model (CLM), <https://doi.org/10.5065/D6FB50WZ>, 2010.

729 Park, S. and Bretherton, C. S.: The University of Washington Shallow Convection and Moist Turbulence Schemes and Their
730 Impact on Climate Simulations with the Community Atmosphere Model, *J. Clim.*, 22, 3449–3469,
731 <https://doi.org/10.1175/2008JCLI2557.1>, 2009.

732 Pham, D. T.: Stochastic Methods for Sequential Data Assimilation in Strongly Nonlinear Systems, *Mon. Wea. Rev.*, 129,
733 1194–1207, [https://doi.org/10.1175/1520-0493\(2001\)129<1194:SMFSDA>2.0.CO;2](https://doi.org/10.1175/1520-0493(2001)129<1194:SMFSDA>2.0.CO;2), 2001.

734 Putman, W. M. and Lin, S.-J.: Finite-volume transport on various cubed-sphere grids, *Journal of Computational Physics*, 227,
735 55–78, <https://doi.org/10.1016/j.jcp.2007.07.022>, 2007.

736 Rashid, H. A., Hendon, H. H., Wheeler, M. C., and Alves, O.: Prediction of the Madden–Julian oscillation with the POAMA
737 dynamical prediction system, *Clim Dynam*, 36, 649–661, <https://doi.org/10.1007/s00382-010-0754-x>, 2011.

738 Raymond, D. J. and Fuchs, Ž.: Moisture Modes and the Madden–Julian Oscillation, *Journal of Climate*, 22, 3031–3046,
739 <https://doi.org/10.1175/2008JCLI2739.1>, 2009.

740 Reynolds, R. W., Smith, T. M., Liu, C., Chelton, D. B., Casey, K. S., and Schlax, M. G.: Daily High-Resolution-Blended
741 Analyses for Sea Surface Temperature, *Journal of Climate*, 20, 5473–5496, <https://doi.org/10.1175/2007JCLI1824.1>, 2007.

742 Rousseeuw, P.: Silhouettes - a Graphical Aid to the Interpretation and Validation of Cluster-Analysis, *J. Comput. Appl. Math.*,
743 20, 53–65, [https://doi.org/10.1016/0377-0427\(87\)90125-7](https://doi.org/10.1016/0377-0427(87)90125-7), 1987.

744 Rui, H. and Wang, B.: Development Characteristics and Dynamic Structure of Tropical Intraseasonal Convection Anomalies,
745 *Journal of the Atmospheric Sciences*, 47, 357–379, [https://doi.org/10.1175/1520-0469\(1990\)047<0357:DCADSO>2.0.CO;2](https://doi.org/10.1175/1520-0469(1990)047<0357:DCADSO>2.0.CO;2),
746 1990a.

747 Rui, H. and Wang, B.: Development Characteristics and Dynamic Structure of Tropical Intraseasonal Convection Anomalies,
748 *Journal of the Atmospheric Sciences*, 47, 357–379, [https://doi.org/10.1175/1520-0469\(1990\)047<0357:DCADSO>2.0.CO;2](https://doi.org/10.1175/1520-0469(1990)047<0357:DCADSO>2.0.CO;2),
749 1990b.

750 Vitart, F.: Madden—Julian Oscillation prediction and teleconnections in the S2S database, *Q.J.R. Meteorol. Soc.*, 143, 2210–
751 2220, <https://doi.org/10.1002/qj.3079>, 2017.

752 Vitart, F. and Molteni, F.: Dynamical Extended-Range Prediction of Early Monsoon Rainfall over India, *Mon. Weather Rev.*,
753 137, 1480–1492, <https://doi.org/10.1175/2008MWR2761.1>, 2009.

754 Vitart, F. and Molteni, F.: Simulation of the Madden-Julian Oscillation and its teleconnections in the ECMWF forecast system,
755 *Q. J. R. Meteorol. Soc.*, 136, 842–855, <https://doi.org/10.1002/qj.623>, 2010.

756 Vitart, F., Ardilouze, C., Bonet, A., Brookshaw, A., Chen, M., Codorean, C., Déqué, M., Ferranti, L., Fucile, E., Fuentes, M.,
757 Hendon, H., Hodgson, J., Kang, H.-S., Kumar, A., Lin, H., Liu, G., Liu, X., Malguzzi, P., Mallas, I., Manoussakis, M.,
758 Mastrangelo, D., MacLachlan, C., McLean, P., Minami, A., Mladek, R., Nakazawa, T., Najm, S., Nie, Y., Rixen, M., Robertson,

759 A. W., Ruti, P., Sun, C., Takaya, Y., Tolstykh, M., Venuti, F., Waliser, D., Woolnough, S., Wu, T., Won, D.-J., Xiao, H.,
760 Zaripov, R., and Zhang, L.: The Subseasonal to Seasonal (S2S) Prediction Project Database, *B Am Meteorol Soc*, 98, 163–
761 173, <https://doi.org/10.1175/BAMS-D-16-0017.1>, 2017.

762 Waliser, D. E., Lau, K. M., Stern, W., and Jones, C.: Potential Predictability of the Madden–Julian Oscillation, *B Am Meteorol*
763 *Soc*, 84, 33–50, <https://doi.org/10.1175/BAMS-84-1-33>, 2003.

764 Wang, B.: Dynamics of Tropical Low-Frequency Waves: An Analysis of the Moist Kelvin Wave, *Journal of the Atmospheric*
765 *Sciences*, 45, 2051–2065, [https://doi.org/10.1175/1520-0469\(1988\)045<2051:DOTLFW>2.0.CO;2](https://doi.org/10.1175/1520-0469(1988)045<2051:DOTLFW>2.0.CO;2), 1988.

766 Wang, B. and Lee, S.-S.: MJO Propagation Shaped by Zonal Asymmetric Structures: Results from 24 GCM Simulations,
767 *Journal of Climate*, 30, 7933–7952, <https://doi.org/10.1175/JCLI-D-16-0873.1>, 2017.

768 Wang, B., Chen, G., and Liu, F.: Diversity of the Madden-Julian Oscillation, *SCIENCE ADVANCES*, 2019.

769 Wang, W., Hung, M.-P., Weaver, S. J., Kumar, A., and Fu, X.: MJO prediction in the NCEP Climate Forecast System version
770 2, *Clim Dyn*, 42, 2509–2520, <https://doi.org/10.1007/s00382-013-1806-9>, 2014.

771 Wheeler, M. C. and Hendon, H. H.: An All-Season Real-Time Multivariate MJO Index: Development of an Index for
772 Monitoring and Prediction, *Monthly Weather Review*, 132, 1917–1932, [https://doi.org/10.1175/1520-0493\(2004\)132<1917:AARMMI>2.0.CO;2](https://doi.org/10.1175/1520-0493(2004)132<1917:AARMMI>2.0.CO;2), 2004a.

774 Wheeler, M. C. and Hendon, H. H.: An All-Season Real-Time Multivariate MJO Index: Development of an Index for
775 Monitoring and Prediction, *Mon. Wea. Rev.*, 132, 1917–1932, [https://doi.org/10.1175/1520-0493\(2004\)132<1917:AARMMI>2.0.CO;2](https://doi.org/10.1175/1520-0493(2004)132<1917:AARMMI>2.0.CO;2), 2004b.

777 Wheeler, M. C., Hendon, H. H., Cleland, S., Meinke, H., and Donald, A.: Impacts of the Madden–Julian Oscillation on
778 Australian Rainfall and Circulation, *Journal of Climate*, 22, 1482–1498, <https://doi.org/10.1175/2008JCLI2595.1>, 2009.

779 Wu, C.-H. and Hsu, H.-H.: Topographic Influence on the MJO in the Maritime Continent, *J. Clim.*, 22, 5433–5448,
780 <https://doi.org/10.1175/2009JCLI2825.1>, 2009.

781 Wu, X., Deng, L., Song, X., Vettoretti, G., Peltier, W. R., and Zhang, G. J.: Impact of a modified convective scheme on the
782 Madden-Julian Oscillation and El Niño–Southern Oscillation in a coupled climate model: MJO AND ENSO SIMULATED
783 BY A COUPLED GCM, *Geophys. Res. Lett.*, 34, <https://doi.org/10.1029/2007GL030637>, 2007.

784 Xiang, B., Zhao, M., Jiang, X., Lin, S.-J., Li, T., Fu, X., and Vecchi, G.: The 3–4-Week MJO Prediction Skill in a GFDL
785 Coupled Model, *J Climate*, 28, 5351–5364, <https://doi.org/10.1175/JCLI-D-15-0102.1>, 2015.

786 Xiang, B., Harris, L., Delworth, T. L., Wang, B., Chen, G., Chen, J.-H., Clark, S. K., Cooke, W. F., Gao, K., Huff, J. J., Jia,
787 L., Johnson, N. C., Kapnick, S. B., Lu, F., McHugh, C., Sun, Y., Tong, M., Yang, X., Zeng, F., Zhao, M., Zhou, L., and Zhou,
788 X.: S2S Prediction in GFDL SPEAR: MJO Diversity and Teleconnections, *B Am Meteorol Soc*, 103, E463–E484,
789 <https://doi.org/10.1175/BAMS-D-21-0124.1>, 2022.

790 Yang, C., Liu, J., and Xu, S.: Seasonal Arctic Sea Ice Prediction Using a Newly Developed Fully Coupled Regional Model
791 With the Assimilation of Satellite Sea Ice Observations, *J Adv Model Earth Syst*, 12, e2019MS001938,
792 <https://doi.org/10.1029/2019MS001938>, 2020.

793 Zeng, L., Bao, Q., Wu, X., He, B., Yang, J., Wang, T., Liu, Y., Wu, G., and Liu, Y.: Impacts of humidity initialization on MJO
794 prediction: A study in an operational sub-seasonal to seasonal system, *Atmospheric Research*, 294, 106946,
795 <https://doi.org/10.1016/j.atmosres.2023.106946>, 2023.

796 Zhang, C.: Madden-Julian Oscillation: MADDEN-JULIAN OSCILLATION, *Rev. Geophys.*, 43,
797 <https://doi.org/10.1029/2004RG000158>, 2005.

798 Zhou, L. and Harris, L.: Integrated Dynamics-Physics Coupling for Weather to Climate Models: GFDL SHIELD With In-Line
799 Microphysics, *Geophys. Res. Lett.*, 49, e2022GL100519, <https://doi.org/10.1029/2022GL100519>, 2022.

800 Zhou, L., Lin, S.-J., Chen, J.-H., Harris, L. M., Chen, X., and Rees, S. L.: Toward Convective-Scale Prediction within the Next
801 Generation Global Prediction System, *Bulletin of the American Meteorological Society*, 100, 1225–1243,
802 <https://doi.org/10.1175/BAMS-D-17-0246.1>, 2019.

803